e-JSNM

e-JURNAL SAINS NUKLEAR MALAYSIA
e-NUCLEAR SCIENCE JOURNAL OF MALAYSIA

Volume 37 (No.1) 2025
A scientific journal by Malaysian Nuclear Agency
eISSN 2232-0946

eJURNAL
SAINS NUKLEAR MALAYSIA

VOL. 37 NO. 1 (2025)
eISSN: 2232-0946

Jurnal Sains Nuklear Malaysia (JSNM, Nuclear Science Journal of Malaysia) is published in the months of June and December annually since 1982 by the Malaysian Nuclear Agency (formerly known as PUSPATI, UTN and MINT). This journal provides a platform for researchers, scientists and engineers (RSEs) to publish their research findings and reviews related to nuclear science and technology so that they can be shared with colleagues throughout the world.

As a means to internationalise JSNM, the Board of Editors welcomes scientific, technical and review articles written by members of the scientific community from home and abroad.

Previously a purely traditional printed journal, JSNM is now adapted and available in electronic form, in keeping with demands and rapid development of ICT. This adaptation also translates to ease of accessibility of JSNM for scientific communities as well as to facilitate knowledge sharing among RSEs.

On behalf of the Editorial Board of JSNM, we would like to acknowledge and thank the authors and referees for their significant contributions to the success of this journal and for embracing this new publication format.

Every effort has been made to trace and acknowledge all copyright holders, but if any have been inadvertently overlooked, the publishers would please to make the necessary arrangements at the first opportunity.

Publishing Office
Malaysian Nuclear Agency, Bangi,
43000 Kajang,
Selangor Darul Ehsan,
MALAYSIA
Tel : +6 03 8911 2000
Fax : +6 03 8911 2154

Website
http://jsnm.nuclearmalaysia.gov.my

TABLE OF CONTENTS

NO	ARTICLE	PAGE
1.	**STRUCTURE, MORPHOLOGY AND HYDROGEN STORAGE PROPERTIES OF TI-MN ALLOY SYNTHESIZED BY MECHANICAL ALLOYING TECHNIQUE** *Julie Andrianny Murshidi*	**1 – 11**
2	**ENHANCING STEEL RADIOGRAPHY TESTING: A NEW X-RAY EXPOSURE CHART WITH PHOSPHORUS-BASED IMAGING PLATES** *Sapizah Rahim, Syaza Adani Ahmad Shahrul Aimee, Siti Nur Najihah Meor Kamarulzaman, Ilhan Shah Amran, Khairul Anuar Mohd Salleh, Arshad Yassin and Mohd Junaidi Jaapar*	**12 – 20**
3.	**EFFECTS OF CHRONIC GAMMA IRRADIATION ON CASSAVA VAR. *UBI KUNING*** *Muniroh Md Saad, Norazlina Noordin, Mustapha Akil, Shakinah Salleh, Norhafiz Talib[1], Zaki Hussain, Muhammad Abu Bakar, Muhammad Syamim Abdul Rahim and Noor Shaireen Shahira Khalid*	**21 – 32**
4.	**PREDICTION OF RTP FUEL SOURCE TERM AND DECAY HEAT IN SURROUNDING MATERIALS** *Mohamad Hairie Rabir, Mark Dennis Usang, Muhammad Khairul Ariff Mustafa, Julia Abdul Karim and Mohamad Amirudin Mohamad Rosli*	**33 – 49**
5.	**ANALYSIS OF CYCLE LENGTH FOR HIGH-FISSILE-DENSITY FUEL IN HTR-MMR** *Mohamad Hairie Rabir, Mark Dennis Usang and Julia Abdul Karim*	**50 – 60**
6.	**RECOVERY OF NEODYMIUM AND DYSPROSIUM FROM ACETIC ACID LEACHING SOLUTION OF XENOTIME BY SOLVENT EXTRACTION** *Khaironie Mohamed Takip, Roshasnorlyza Hazan, Nur Aqilah Sapiee, Jacqueline Kones, Norhazirah Azhar, Wilfred Paulus, Nor Asniza Ariffin and Muhammad Faiz Fadzel*	**61 – 68**

Jurnal Sains Nuklear Malaysia, 2025, 37(No. 1): 1 – 11
ISSN: 2232-0946

STRUCTURE, MORPHOLOGY AND HYDROGEN STORAGE PROPERTIES OF TI-MN ALLOY SYNTHESIZED BY MECHANICAL ALLOYING TECHNIQUE

Julie Andrianny Murshidi

Materials Technology Group
Industrial Technology Division, Malaysian Nuclear Agency
Bangi, 43000 Kajang, Selangor
Corresponding Author: julie@nm.gov.my

ABSTRACT

Ti-Mn alloy compounds with the composition $TiMn_2$, $Ti_{0.97}Zr_{0.019}Mn_{1.5}Cr_{0.57}$ *and* $Ti_{0.7875}Zr_{0.2625}Mn_{0.8}Cr_{1.2}$ *were synthesised by mechanical alloying technique. An amorphous Ti-Mn alloy was formed when the starting reagents were mechanical alloying for 40 h. The corresponding crystalline phase TiMn was formed when the amorphous alloy was annealed at 800℃. The addition of a process control agent (Toluene) leads to the formation of a carbide phase (TiC) in the samples. The presence of impurities, carbide (TiC) and oxide (TiO) phases resulted a decrease in C14 laves phase wt.% in the synthesised samples. Only 37.24, 31.5 and 32.81 wt.% C14 phase were formed in* $TiMn_2$, $Ti_{0.97}Zr_{0.019}Mn_{1.5}Cr_{0.57}$ *and* $Ti_{0.7875}Zr_{0.2625}Mn_{0.8}Cr_{1.2}$ respectively. *The result also showed that the theoretical value of 1.9 hydrogen wt.% could not be reached by these samples.*

Keywords: Mechanical Alloying, Structure, Morphology, Hydrogen Storage

ABSTRAK

Sebatian aloi Ti-Mn dengan komposisi $TiMn_2$, $Ti_{0.97}Zr_{0.019}Mn_{1.5}Cr_{0.57}$ *and* $Ti_{0.7875}Zr_{0.2625}Mn_{0.8}Cr_{1.2}$ *telah disintesis dengan teknik pengaloian secara mekanikal. Aloi Ti-Mn amorfus telah terbentuk apabila reagen permulaan dialoikan secara mekanikal selama 40 jam. Fasa kristal yang sepadan dengan TiMn terbentuk apabila aloi amorfus disepuhlindapkan pada suhu 800℃. Penambahan agen kawalan proses (Toluene) membawa kepada pembentukan fasa karbida (TiC) dalam sampel. Kehadiran fasa bendasing, karbida (TiC) dan oksida (TiO) mengakibatkan penurunan fasa laves C14 wt.% dalam sampel yang disintesis. Hanya 37.24, 31.5 dan 32.81 wt.% fasa C14 terbentuk di dalam* $TiMn_2$, $Ti_{0.97}Zr_{0.019}Mn_{1.5}Cr_{0.57}$ *and* $Ti_{0.7875}Zr_{0.2625}Mn_{0.8}Cr_{1.2}$ *masing-masing. Keputusan juga menunjukkan bahawa nilai teori 1.9 hidrogen wt.% tidak dapat dicapai oleh sampel ini.*

Kata kunci: Pengaloian Mekanikal, Struktur, Morfologi, Penstoran Hidrogen

INTRODUCTION

Much research has been undertaken to investigate the hydrogen storage properties of various types of metal hydride families such as Mg-based systems, BCC alloys and intermetallic systems (AB, AB_2 (Laves phase), AB_3 and AB_5) (Nobuko et. al 2017; Nivedhitha et. al 2024; Lototskyy et. al 2015). Intermetallic systems often consist of a stable hydride forming element with an element forming a nonstable hydride.For AB_2, the systems are based on two Laves phases' crystal structures. The crystal structures can be hexagonal, C14 ($MgZn_2$ type) or cubic, C15 ($MgCu_2$ type) (Nobuko et. al 2017; Lototskyy et. al 2015). In these systems the A elements are usually Ti, Zr, Hf, Th or a lanthanide, whilst the B elements can be a variety of transition and non-transition metals.

At the present time AB_2 intermetallic compounds do not satisfy the requirements for mobile storage due to low gravimetric storage capacities (< 2 wt.%) and often high material cost. The storage capacity limitation is less important for stationary storage applications including thermodynamic devices (refrigerator and air conditioner) (Nobuko et. al 2017), fuel cell applications (Charbonnier et. al 2021; Lototskyy et. al 2015) and energy storage units in remote region (Nobuko et. al 2017; Lototskyy et. al 2015). In addition, there are no weight problems in using heavy hydrogen storage tanks if hydrogen is used as a future fuel or fuel additive for sea transportation (because the extra weight can be used to provide ballast to keep the ship stable) (Güther, V. et. Al 1995; Fiori C. et. al, 2015). An inexpensive intermetallic system with the requisite sorption pressure at a desired temperature with adequate kinetics has the potential to be a hydrogen storage material for these markets. The objective of this study was to synthesise and to investigate the properties of TiMn alloys as suitable candidates for material-based hydrogen storage (hydride materials).

EXPERIMENTAL

The starting materials were Ti (Aldrich, 99.7%, -100 mesh), Zr (Aldrich, 99.7%, -100 mesh), Mn (Aldrich, 99.99%) and Cr (Aldrich, 99+%, -325 mesh). Three alloys of nominal composition $TiMn_2$, $Ti_{0.97}Zr_{0.019}Mn_{1.5}Cr_{0.57}$ and $Ti_{0.7875}Zr_{0.2625}Mn_{0.8}Cr_{1.2}$ were prepared by mechanical alloying the starting materials with toluene in a custom-made ball milling canister (650 cm^3 internal volume) attached to a Glen Mills Turbula T2C shaker-mixer. Toluene was used as a process control agent. Milling was performed under a high purity argon atmosphere using a ball-to-powder (mass) ratio of 12:1 with balls of 7.9 mm and 12.7 mm diameter and milling time of 40 h. The as milled samples were removed from the canister in a glove box under argon. The samples were put into the 316 stainless steel sample cell and annealed at 800°C under vacuum for 3h.

The lattice parameter of the alloy before and after hydrogenation was determined by X-Ray Diffraction (XRD) using a Bruker D8 Advance diffractometer (CuKa radiation) with a 2θ range of 30 - 100° using 0.02° steps and a 0.8 s count time per step with operating conditions of 40 kV and 40 mA. Samples were loaded into XRD low background sample holders in an argon glove box and sealed within a poly(methylmethacrylate) (PMMA) air-tight holder to prevent oxygen/moisture contamination during data collection. The structural parameters were refined from the diffraction data using Rietveld refinement in TOPAS (Bruker AXS, Karlsruhe, Germany) via a fundamental parameters approach. Microstructural observations of as-received and hydrogen cycled alloys were conducted on a Philips XL-30 Scanning Electron Microscopy (SEM) using a secondary electron detector operating at 15 keV. The microscope was coupled with an Oxford Instruments energy dispersive X-Ray spectrometer (EDS) for elemental analysis. Samples were briefly exposed (<1 – 2 min) to air and were not coated with gold prior to imaging in the SEM. The hydrogen sorption properties of the alloy were determined using a custom-built automated Sieverts apparatus (details can be found elsewhere (Marangio, F. et. Al 2011). Before any pressure-composition isotherm (PCI) measurements were undertaken the sample was first evacuated for 1 h at 25 °C to remove any adsorbed gas. Activation of the alloy was then undertaken by first introducing 90 – 96 bars of hydrogen into the sample chamber at room temperature for 1 h, followed by an evacuation step. This hydrogen absorption/ desorption activation cycle was undertaken 3 times. After completion of the activation process, the residual hydrogen within the sample was removed via evacuation at room temperature for 24 h.

RESULTS AND DISCUSSION

Fig. 1 (left) shows that after 12 h of milling, both Ti and Mn peaks were still present. The diffraction peaks are slightly broader compare to those after milling for 2 h. TiC peaks were observed in the XRD pattern due to addition of toluene during milling process. TiC and TiO phases have similar major XRD peaks, so those denoted in Fig. 1 (left) most likely represent the presence of a combination of both TiC and TiO in the sample. After 40 h milling, the sample became quite nanocrystalline. All peaks except the strongest peak of Mn become nearly invisible. The position of the remaining peak of Mn was shifted to a lower angle. The as-milled $TiMn_2$ sample was then annealed at 800°C under vacuum for 3 hours. The XRD pattern shown in Fig. 1 (right) consists of peaks related to $TiMn_2$, TiC, TiO and Mn. The $TiMn_2$ phase was easily indexed on the basis of the hexagonal C14-Laves phases ($P6_3\ /\ mmc$ space group). The calculated lattice parameters determined by Rietveld analysis are listed in Table 1. This result showed that the crystalline phase of Ti-Mn could be achieved through annealing of its milled powder. This is consistent with previous study of synthesising crystalline $Ti_{50}Mn_{50}$ alloy by milling for 40 h and annealing at 700 - 900°C (Chen, C. C. et. al 1993). Annealing was also reported to increase the homogeneity of the crystal structure of the sample (Gamo, T. et. al 1995).

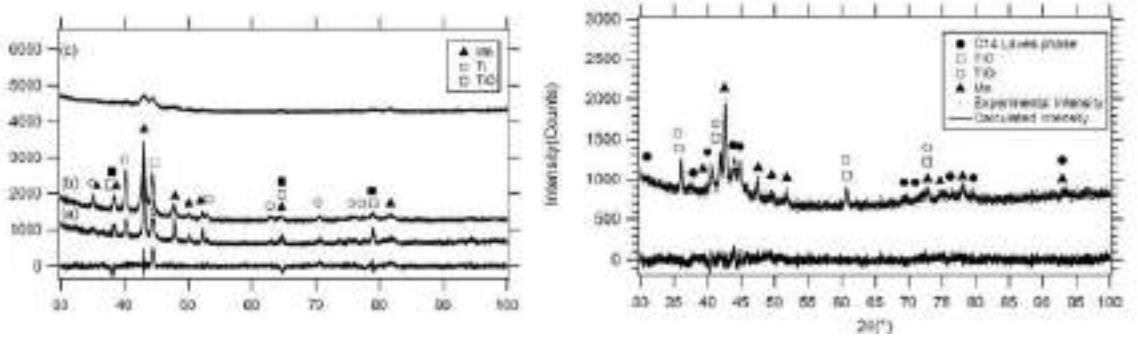

Figure 1: XRD pattern of as-milled $TiMn_2$ powders using BPR of 12:1 at (a) 2 h, (b) 12 h and (c) 40 h milling times (left) and annealed $TiMn_2$ at 800°C (right).

During mechanical alloying, powder particles are subjected to high-energy collision, which causes the powder particles to be cold-welded together and fractured. The essential condition for a successful mechanical alloying process is the balance between cold-welding and fracturing. However, this balance may not be obtained by the milling process itself, especially when soft materials are used. For such cases, cold welding among powder particles and between powder particles and milling tools becomes a serious problem. In order to obtain the balance between the welding and fracturing, a PCA is added in the milling process. The PCA adsorbs on the surface of the powder particles and minimizes the cold-welding effect (Suryanarayana, C. 2001). It is known that Mn is much softer and is more easily to be cold welded to the milling tools compare to Ti. Brinell hardness reported for Ti and Mn are 716 MNm^{-2} and 196 MNm^{-2} respectively. To avoid this, toluene was used as a PCA. However, the addition of toluene resulted in the formation of TiC in the sample. Hydrocarbon PCAs have been reported to introduce carbon and/or oxygen into the powder particles, resulting in the formation of carbides and oxides which are uniformly dispersed in the matrix.

Table 1: Rietveld analysis for phase composition and lattice parameter calculated from XRD patterns in Fig. 1 and 4). Mathematical fitting uncertainties are provided (2 standard deviations).

Alloys	Annealed (wt.%)		Lattice parameters		
			a(nm)	c(nm)	V(nm^3)
$TiMn_2$ (BPR 12:1)	C14	37.24±0.5	0.4821	0.7856	0.1581
	TiO/TiC	22.16±0.5			
	Mn	40.59±0.5			
$Ti_{0.97}Zr_{0.019}Mn_{1.5}Cr_{0.57}$	C14	31.5±1.2	0.4837	0.7892	0.1600
	TiO/TiC	10.31±0.8			
	Mn	58.19±1.6			
$Ti_{0.7875}Zr_{0.2625}Mn_{0.8}Cr_{1.2}$	C14	32.81±0.5	0.4859	0.7940	0.1623
	TiO/TiC	16.41±0.7			
	Cr	39.98±0.5			
	Zr	10.79±0.5			
$TiMn_2$ C14 Laves phase PDF No. 07-0133	-	-	0.4825	0.7917	0.1596

An XRD pattern of the starting Ti powder (Fig. 2) also revealed that a minor oxide phase already presents in the purchased product. Ti powder is known to be more reactive with oxygen when in extremely small particle size (in this case -100 mesh powder) (Suryanarayana, C. 2001). The strongest peak in the starting Ti powder at 36.6° could not be indexed to any known pure Ti element or oxide and is an unknown component. This indicates that there could be an impurity in the Ti starting powder. As a result of these impurity, carbide and oxide phases, the level of Ti available to form $TiMn_2$ alloy was reduced and a high level of Mn was left in the sample. Based on Rietveld analysis in Table 1, only 37.24 wt.% $TiMn_2$ phase was formed in the sample.

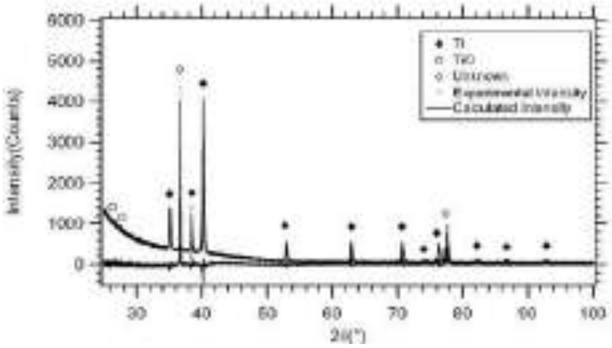

Figure 2:.XRD pattern of starting powder Ti.

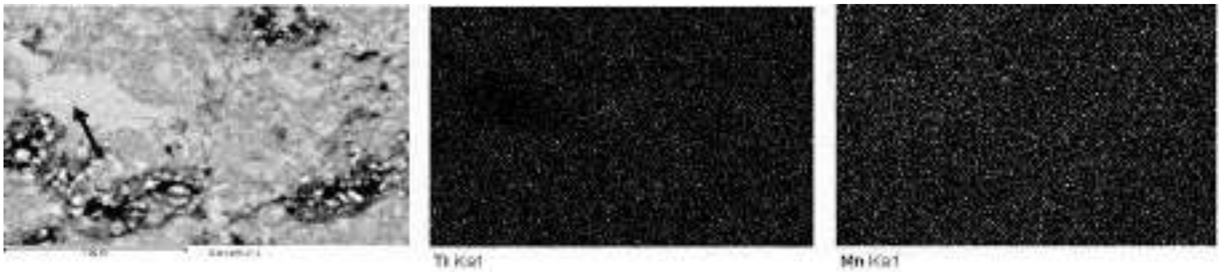

Figure 3: BF image and the corresponding EDS elemental mapping of $TiMn_2$ (bright region is shown by the black arrow)

Fig. 3 of BF image shows no sign of a lamellae structure. At the beginning of mechanical alloying, different elemental powder particles are partially mixed and large blocks containing coarse layers have formed (Mahboubi, S. et. al 2017). Formation of a coarse lamellae structure of initial powders may be due to low plastic deformation. Continuous cold welding and fracturing result coarse layers to be fractured and flattened and subsequently fresh metal surfaces welded together. This results in formation of fine layered structure and inter-diffusion of elements across layers. With further milling up to 40 h, the layers became hardly detectable. The elemental mapping of the sample shows the characteristic energies of Ti and Mn. Both elements are distributed homogeneously throughout the sample except the bright region. The brighter region contains more Mn and less Ti than the darker region. This observation indicates that there may not be enough Ti content to diffuse in the (Ti, Mn) matrix forming different contrast in the sample.

Fig. 4 show the XRD patterns of $Ti_{0.97}Zr_{0.019}Mn_{1.5}Cr_{0.57}$ and $Ti_{0.7875}Zr_{0.2625}Mn_{0.8}Cr_{1.2}$ samples respectively prepared by mechanical alloying the starting reagents using a BPR of 12:1 for 40 hours. 3 drops of toluene were added to the starting reagents during milling. Then the as-milled samples were annealed at 800°C under vacuum for 3 hours. Both XRD patterns consist of peaks related to $TiMn_2$, TiC, TiO and Mn. As a result of impurity, carbide and oxide phases' presence in these samples, the level of Ti available to form $TiMn_2$ alloy were reduced. Based on Rietveld analysis in Table 1, only 31.5 wt.% and 32.81 wt.% $TiMn_2$ phase was formed in $Ti_{0.97}Zr_{0.019}Mn_{1.5}Cr_{0.57}$ and $Ti_{0.7875}Zr_{0.2625}Mn_{0.8}Cr_{1.2}$ respectively. For $Ti_{0.7875}Zr_{0.2625}Mn_{0.8}Cr_{1.2}$, due to its low wt.% $TiMn_2$ phase formed and the high level of substitute elements used (Zr and Cr), only limited levels of partially substitution could take place in the sample. As a result, peaks related to Cr and Zr phases were still detected in this sample as shown in Fig. 4. The effects of partial substitution of Zr for Ti and Cr for Mn are shown in Table 1. With increasing Zr and Cr content, the lattice parameter of the C14- Laves phases were also increased. This is due to the atom radius of Zr and Cr are bigger than that of Mn.

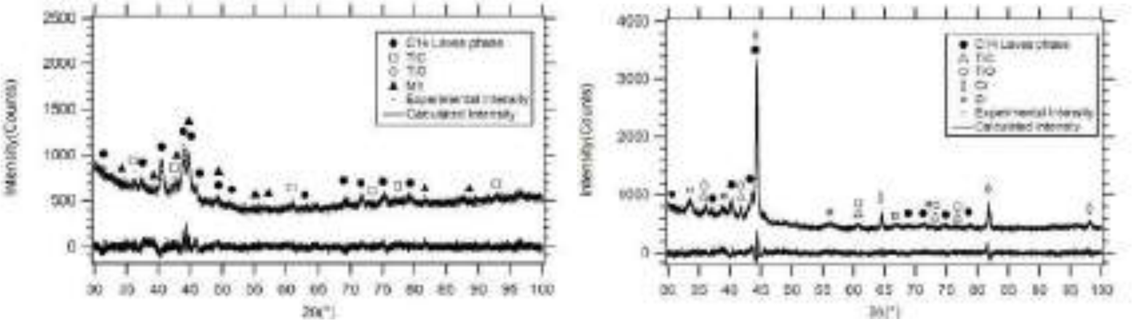

Figure 4: XRD pattern of $Ti_{0.97}Zr_{0.019}Mn_{1.5}Cr_{0.57}$ (left) and $Ti_{0.7875}Zr_{0.2625}Mn_{0.8}Cr_{1.2}$ (right).

Fig. 5 shows the BF image of the sample$Ti_{0.97}Zr_{0.019}Mn_{1.5}Cr_{0.57}$ and its corresponding EDS elemental mapping. All elements are distributed homogeneously throughout the sample except the bright region. The brighter region contains more Cr, Mn and less Ti than the darker region. This indicates that the alloy was composed of the C14 Laves phase (dark region) and some impurity phase of Mn and Cr (bright region). This result is also similar with sample $Ti_{0.7875}Zr_{0.2625}Mn_{0.8}Cr_{1.2}$ as shown in Fig. 6. However, Zr element was also detected in this sample due to high level of Zr in sample $Ti_{0.7875}Zr_{0.2625}Mn_{0.8}Cr_{1.2}$ compare to $Ti_{0.97}Zr_{0.019}Mn_{1.5}Cr_{0.57}$.

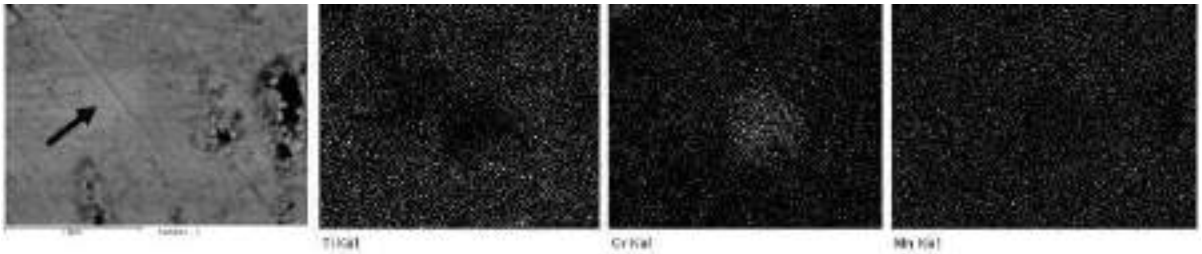

Figure 5: BF image and the corresponding EDS elemental mapping of $Ti_{0.97}Zr_{0.019}Mn_{1.5}Cr_{0.57}$ (bright region is shown by the black arrow)

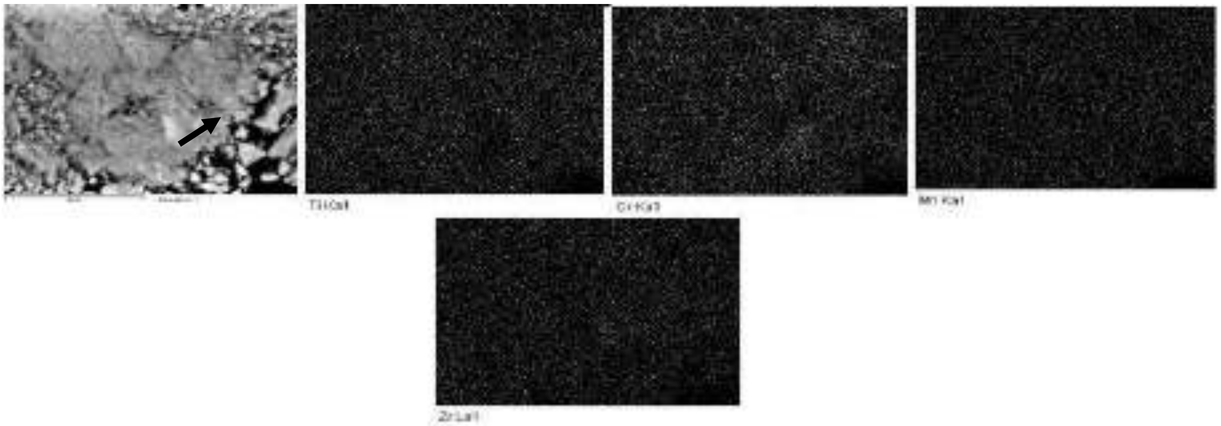

Figure 6: BF image and the corresponding EDS elemental mapping of $Ti_{0.7875}Zr_{0.2625}Mn_{0.8}Cr_{1.2}$ (bright region is shown by the black arrow).

EDS data verifies the presence of high quantities of Ti and Mn in all samples (Fig. 7a, b and c). EDS also showed the existence of Fe, Cr and Ni for all samples, as a result of an excessive wear of the milling tools. Zr and Cr are the results of partial substitution of Ti and Mn in sample $Ti_{0.97}Zr_{0.019}Mn_{1.5}Cr_{0.57}$ (Fig. 7b) and $Ti_{0.7875}Zr_{0.2625}Mn_{0.8}Cr_{1.2}$ (Fig. 7c). Cr contents are higher in Fig. 7c due to high level of Cr in sample $Ti_{0.7875}Zr_{0.2625}Mn_{0.8}Cr_{1.2}$ compare to sample $Ti_{0.97}Zr_{0.019}Mn_{1.5}Cr_{0.57}$. C comes from using toluene as a PCA.

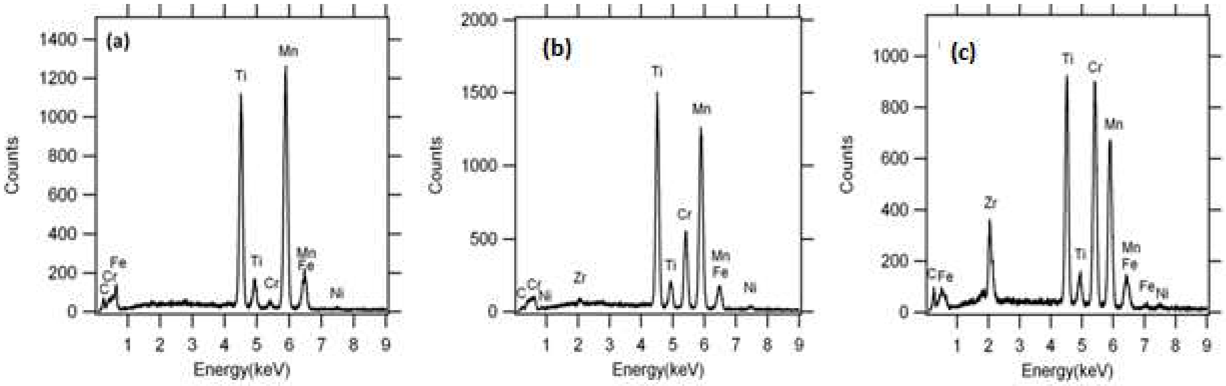

Figure 7: EDS spectra of (a) $TiMn_2$, (b) $Ti_{0.97}Zr_{0.019}Mn_{1.5}Cr_{0.57}$ and (c) $Ti_{0.7875}Zr_{0.2625}Mn_{0.8}Cr_{1.2}$.

Table 2 show the maximum hydrogen wt.% of sample $TiMn_2$, $Ti_{0.97}Zr_{0.019}Mn_{1.5}Cr_{0.57}$ and $Ti_{0.7875}Zr_{0.2625}Mn_{0.8}Cr_{1.2}$ respectively. Maximum hydrogen absorbed in $TiMn_2$, $Ti_{0.7875}Zr_{0.2625}Mn_{0.8}Cr_{1.2}$ and $Ti_{0.97}Zr_{0.019}Mn_{1.5}Cr_{0.57}$ sample were only 0.15 wt.%, 0.19 wt.% and 0.34 wt.% respectively due to impurities phases. It was clear that theoretical value of 1.9 hydrogen wt.% would not be reached by these samples. High energy milling and longer milling time lead to heavy deformation of samples and high oxidisation of sample (Suryanarayana, C. 2001). It is believed that these crystal deformities and together with impurity phases (oxides, carbides, MnCrZr) both contribute to the low hydrogen weight capacity achieved in these samples.

Table 2: Hydrogen contents in $TiMn_2$, $Ti_{0.97}Zr_{0.019}Mn_{1.5}Cr_{0.57}$ and $Ti_{0.7875}Zr_{0.2625}Mn_{0.8}Cr_{1.2}$ samples.

Cycle	Hydrogen Absorption in $TiMn_2$	Maximum hydrogen wt.%
1	Initial pressure of 96.30 bar was applied at RT for 1 h and the final pressure was 47.98 bar.	0.15
2	Initial pressure of 94.35 bar was applied at RT for 1 h and the final pressure was 47.10 bar.	0.15
3	Initial pressure of 94.68 bar was applied at RT for 1 h and the final pressure was 47.18 bar.	0.12
Cycle	Hydrogen contents in $Ti_{0.97}Zr_{0.019}Mn_{1.5}Cr_{0.57}$	Maximum hydrogen wt.%
1	Initial pressure of 96.19 bar was applied at RT for 1 h and the final pressure was 49.29 bar.	0.19
2	Initial pressure of 96.74 bar was applied at RT for 1 h and the final pressure was 49.53 bar.	0.17
3	Initial pressure of 96.88 bar was applied at RT for 1 h and the final pressure was 49.52 bar.	0.18
Cycle	Hydrogen contents in $Ti_{0.7875}Zr_{0.2625}Mn_{0.8}Cr_{1.2}$	Maximum hydrogen wt.%
1	Initial pressure of 90.81 bar was applied at RT for 1 h and the final pressure was 42.25 bar.	0.32
2	Initial pressure of 90.65 bar was applied at RT for 1 h and the final pressure was 42.29 bar.	0.34
3	Initial pressure of 90.54 bar was applied at RT for 1 h and the final pressure was 42.12 bar.	0.28

From the hydrogen absorption measurement, the kinetics of the samples (Fig. 8) was determined. The kinetics of hydrogen absorption was measured by recording wt.% data at room temperature. It was found that the sample had very fast kinetics, with alloys reaching hydrogen absorption equilibrium within 30 minutes.

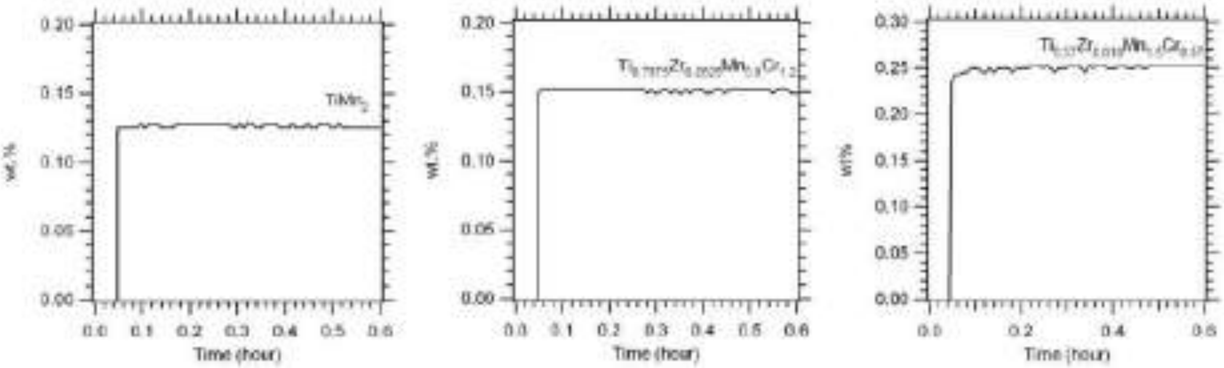

Figure 8: Hydrogenation kinetics on absorption at room temperature for $TiMn_2$, $Ti_{0.7875}Zr_{0.2625}Mn_{0.8}Cr_{1.2}$ and $Ti_{0.97}Zr_{0.019}Mn_{1.5}Cr_{0.57}$ samples after three activation cycles.

CONCLUSION

Ti-Mn alloy compounds with the composition $TiMn_2$, $Ti_{0.97}Zr_{0.019}Mn_{1.5}Cr_{0.57}$ and$Ti_{0.7875}Zr_{0.2625}Mn_{0.8}Cr_{1.2}$ have been synthesised. A nanocrystalline Ti-Mn alloy was formed when the starting reagents were mechanical alloying for 40 h, using a ball-to-powder (mass) ratio of 12:1 and annealed at 800°C. The addition of PCA leads to the formation of carbide phase (TiC) in the samples. The presence of impurity, carbide (TiC) and oxide (TiO) phases resulted a decrease in C14 laves phase wt.% in the synthesised samples. Only 37.24, 31.5 and 32.81 wt.% C14 phase were formed in $TiMn_2$, $Ti_{0.97}Zr_{0.019}Mn_{1.5}Cr_{0.57}$ and $Ti_{0.7875}Zr_{0.2625}Mn_{0.8}Cr_{1.2}$ respectively. The result also showed that the theoretical value of 1.9 hydrogen wt.% could not be reached by these samples. Therefore, for future work, samples with an oxygen scavenger and an effective PCA that will not react with the starting reagents should be studied.

ACKNOWLEDGEMENTS

The author would like to thank the Government of Malaysia for funding and all personnel involved for their direct or indirect support to carry out this project.

REFERENCES

Charbonnier V. , Enoki H. , Asano K. , Kim H. , Sakaki K., (2021), Tuning the hydrogenation properties of $Ti_{1+y}Cr_{2-x}Mn_x$ laves phase compounds for high pressure metal-hydride compressors, *International Journal of Hydrogen* Energy, 46: 36369-36380

Chen, C. C., Chin, Z. H., Perng, T. P., (1993), Preparation and crystallization of $Ti_{50}Mn_{50}$ amorphous alloy, *Materials Science and Engineering: A*, *173*: 381 - 384.

Cingi, M. M., O. Guleryuz, H. Baydogan, M. Cimenoglu, H. Kayali, E.S. (2007), High Cyclic Fatigue Bahaviour of Thermally Oxidized Ti6Al4V Alloy, *Materials Science Forum*, *561/565*: 2179 - 2182.

El-Eskandarany, M.S., (2001), *Mechanical Alloying for Fabrication of Advanced Engineering Materials*, William Andrew Publishing, New York. 142 – 173.

Fiori C., Dell'Era A., Zuccari F., Santiangeli A., D'Orazio A., Orecchini F., (2015), Hydrides for submarine applications: Overview and identification of optimal alloys for air independent propulsion maximization, International Journal of Hydrogen Energy, 40: 11879-11889.

Gamo, T., Moriwaki, Y., Yanagihara, N., Yamashita, T., Iwaki, T., (1985), Formation and properties of titanium-manganese alloy hydrides, *International Journal of Hydrogen Energy*, *10*:39 - 47.

Güther, V.; Otto, A., (1999), Recent developments in hydrogen storage applications based on metal hydrides, *Journal of Alloys and Compounds*, 293 - 295: 889 - 892.

Lototskyy M. , Satya Sekhar B., Muthukumar P., Linkov V., Pollet B. G., (2015), Niche applications of metal hydrides and related thermal management issues, *Journal of Alloys and Compounds*, 645: S117-S122.

Lototskyy, M. V., Tolj, I., Pickering, L., Sita, C., Barbir, F., & Yartys, V. (2017). The use of metal hydrides in fuel cell applications. *Progress in Natural Science: Materials International*, 27(1), 3–20.

Mahboubi, S. A., Karimzadeh F., Enayati M., (2012), Formation mechanism and characterization of nanostructured Ti6Al4V alloy prepared by mechanical alloying, *Materials & Design*, 37: 152-160,

Marangio, F., Pagani, M., Santarelli, M., Calì, M., (2011), Concept of a high pressure PEM electrolyser prototype *International Journal of Hydrogen Energy*, 36: 7807 - 7815.

Mohd N. I., Teuku H., Jonathan G., Abu B., (2022), High-pressure PEM water electrolyser: A review on challenges and mitigation strategies towards green and low-cost hydrogen production, *Energy Conversion and Management* 268(486):115985

Nivedhitha K.S, Beena T., Banapurmath N.R., Umarfarooq M.A., Venkatesh R., Manzoore E. M. S, (2024), Advances in hydrogen storage with metal hydrides: Mechanisms, materials, and challenges, *International Journal of Hydrogen Energy*, 61: 1259-1273.

Nobuko H., Hirotaka A., Tessui Nakagawa., Hiroki Higa., Masayoshi I., Daichi H., Tomohiro T., Itoko S., Kohta A., Yumiko N., Akitoshi F., Shinichi M., (2017), Effect of CO_2 on hydrogen absorption in Ti-Zr-Mn-Cr based AB_2 type alloys, *Journal of Alloys and Compounds*, 705: 507-516

Suryanarayana, C. (2001), Mechanical alloying and milling, *Progress in Materials Science*, 46: 1 - 184.

Villeroy, B., Cuevas, F., Bettembourg, J., Olier, P., Latroche, M., (2006), Influence of the Ti/Zr ratio and the synthesis route on hydrogen absorbing properties of (Ti1−xZrx)Mn1.5V0.5 alloys, *Journal of Physics and Chemistry of Solids*, 67(5-6): 1281–1285.

Jurnal Sains Nuklear Malaysia, 2025, 37(No. 1): 12 – 20
ISSN: 2232-0946

ENHANCING STEEL RADIOGRAPHY TESTING: A NEW X-RAY EXPOSURE CHART WITH PHOSPHORUS-BASED IMAGING PLATES

PENINGKATAN UJIAN RADIOGRAFI KELULI: CARTA DEDAHAN SINAR-X DENGAN PLAT PENGIMEJAN BERASAKAN FOSFOR

Sapizah Rahim[1*], Syaza Adani Ahmad Shahrul Aimee[2], Siti Nur Najihah Meor Kamarulzaman[2], Ilhan Shah Amran[3], Khairul Anuar Mohd Salleh[1], Arshad Yassin[1] and Mohd Junaidi Jaapar[1]

[1]LENDT Group, Industrial Technology Division,
Malaysian Nuclear Agency, 43000 Kajang, Selangor
[2]Faculty of Science and Technology, USIM,
Bandar Baru Nilai, 71800 Nilai, Negeri Sembilan
[3]Faculty of Chemical and Energy Engineering, Universiti Teknologi Malaysia, Johor
*Correspondence author: sapizah@nm.gov.my

ABSTRACT

An exposure chart serves as a critical tool for correlating exposure time with the strength of the radiation source and the thickness of the material being tested. It aims to ensure consistent image quality across various examinations and imaging systems. Traditionally, exposure charts were designed for X-ray machines that utilized film as the imaging medium. However, with the advent of digital imaging, imaging plates (such as those used in Computed Radiography systems) have replaced films, allowing for the creation of digital images. These digital images can be electronically stored, eliminating the need for physical film storage and streamlining image retrieval processes. While digital imaging has significantly advanced the field, comprehensive exposure charts specifically tailored for phosphor imaging plates in industrial applications are still lacking. This study addresses this gap by creating an exposure chart using a steel step wedge and a white imaging plate (equivalent to D7 film) for the Isovolt Titan E x-ray machine. To calibrate the system, we determine the minimum gray value (GVmin) and energy using a copper step wedge at a focal-detector distance of 100 cm and an energy level of 180 kV. Each step wedge is exposed to varying energy levels and constant current until the desired gray value is achieved. Subsequently, we construct an exposure chart based on steel thickness (measured in millimeters). By comparing the film and developed exposure charts, we evaluate their performance using welded plates. The results demonstrate that an exposure chart can indeed be developed for phosphor imaging plates. Furthermore, the computed radiography system significantly reduces exposure time (by approximately 80%), making it quantitatively comparable to conventional film radiography.

Keywords: exposure chart; phosphor imaging plate; steel

ABSTRAK

Carta pendedahan berfungsi sebagai alat penting untuk menghubungkan masa pendedahan dengan kekuatan sumber radiasi dan ketebalan bahan yang diuji. Ia bertujuan untuk memastikan kualiti imej yang konsisten dalam pelbagai pemeriksaan dan sistem imbasan. Secara amnya, carta pendedahan direka untuk mesin sinar-X yang menggunakan filem sebagai medium pengimejan. Namun, plat imbasan (seperti yang digunakan dalam sistem Radiografi Berkomputer) telah menggantikan filem, membolehkan penghasilan imej digital. Imej digital ini boleh disimpan secara elektronik, tiada keperluan untuk penyimpanan filem fizikal dan menyederhanakan proses pengambilan imej. Walaupun imej digital telah berkembang pesat dalam bidang ini, carta pendedahan yang komprehensif yang khusus untuk plat imbasan fosfor dalam aplikasi industri masih kurang. Kajian ini adalah untuk membangunkan carta pendedahan menggunakan baji jenjang dan plat imbasan putih (setara dengan filem D7) untuk mesin sinar-X Isovolt Titan E. Sistem ini ditentukurkan dengan menentukan nilai kelabu minimum (GV_{min}) *dan tenaga menggunakan baji jenjang pada jarak fokus-pengesan 100 cm dan tenaga 180 kV. Setiap baji jenjang keluli dikenakan tahap tenaga yang berbeza dan arus yang tetap sehingga nilai kelabu yang diingini tercapai. Seterusnya, carta pendedahan dibangunkan berdasarkan ketebalan baji jenjang keluli (milimeter). Dengan membandingkan carta pendedahan filem sedia ada dan carta dedahan yang dibangunkan, kami menilai prestasi carta dedahan tersebut menggunakan plat keluli terkimpal. Hasil kajian mendapati bahawa carta pendedahan boleh dibangunkan untuk plat imbasan fosfor. Selain itu, sistem radiografi berkomputer secara ketara mengurangkan masa pendedahan (sekitar 80%), menjadikannya secara kuantitatif sebanding dengan radiografi filem konvensional.*

Kata kunci: carta dedahan; plat pengimejan fosfor; keluli

INTRODUCTION

Computed Radiography (CR) has emerged as a powerful tool in Non-Destructive Testing (NDT), revolutionizing how X-ray images are captured. Unlike film-based radiography, CR employs Photostimulable Phosphor (PSP) imaging plates. These flexible plates absorb X-ray energy during exposure, temporarily storing it within their phosphor layer. After exposure, the plates are scanned using a CR reader, which releases the stored energy and converts it into a digital image. The advantages of CR include rapid image acquisition, cost-effectiveness (due to reusable plates), and the ability to adjust image quality during post-processing. Nowadays, NDT practitioners rely on CR for discontinuity detection and weld inspection, contributing to safer and more efficient Radiographic Testing (RT) processes.

A phosphor imaging plate comprises a thin layer of PSP. This phosphor material has the unique property of absorbing X-ray energy during exposure. When the imaging plate is exposed to X- rays, the phosphor grains within the plate become excited, trapping electrons within the lattice structure of the phosphor material. These trapped electrons remain latent until the second round of illumination occurs. During this second stage, the imaging plate is scanned by a laser beam, which stimulates the trapped electrons, causing them to release their stored energy. The released energy is then converted into a digital image, representing the X-ray exposure pattern captured by the imaging plate. Compared to traditional film-based radiography, CR provides immediate digital results requiring chemical development.

The exposure is determined based on the exposure chart. The chart guides the correct settings and techniques for each RT exposure. When setting up testing equipment for inspections, RT personnel refer to exposure charts to ensure repeatable testing processes. RT personnel can optimize image quality and flaw detection by following exposure guidelines specific to the type of material (such as steel), the X-ray equipment, and the source-to-film distance (SFD). Whether inspecting welds, castings, or other critical components, an exposure chart is vital in maintaining the integrity of industrial structures and equipment. Despite the numerous advantages of CR, NDT practitioners often rely on a trial-and-error approach to determine the correct exposure time during radiographic inspection.

This work aims to meet the RT requirements related to image quality or sensitivity. Therefore, our motivation lies in developing an exposure chart that utilizes phosphor imaging plates as a film replacement for inspecting steel welds in industrial applications. The comparison of exposure time based on film and imaging plates for welded plates is also studied.

METHODOLOGY

Equipment

The computed radiography system used in this study is the 16-bit ADC HD-CR 35 NDT model, along with a 650 gain HV V000121 reader. The imaging plate used is white with a 100 µm laser spot size during scanning. The X-ray machine is the Isovolt Titan E model with a voltage range of 5 to 225 kV and a focal spot size of 3.0 mm. The duplex wire used is based on ASTM E2022 (ISO 19232-5), and the copper step wedge is based on ASTM 2446.

Experimental

The Basic Spatial Resolution (SR_b) for the CR system is measured using a duplex wire Image Quality Indicator (IQI) and an X-ray machine with a focal spot-detector distance of 120 cm (Figure 1). Exposure at 90 kV without a filter in front of the X-ray beam is performed vertically and horizontally against the scanning angle until a 50-80% gray value on the duplex wire is achieved. The minimum gray value is determined based on exposure to a copper step wedge with 180 kV X-ray beam energy using a white imaging plate with a focal spot-detector distance of 1.0 meter (Figure 2). A graph of normalized SNR against gray value is plotted, and the minimum gray value for testing class A (SNR~70) is determined. This value is then used as a reference for exposing a steel step wedge with varying step thicknesses at different X-ray beam energies and currents to obtain the correct exposure values. The obtained exposure values are then plotted against the steel thickness for each voltage (beam energy) used at an SNR value of 70 using a white imaging plate. To validate the developed exposure chart, a welded plate specimen is inspected with exposure time based on the developed exposure chart. This exposure time is then compared with the exposure time required by film radiography.

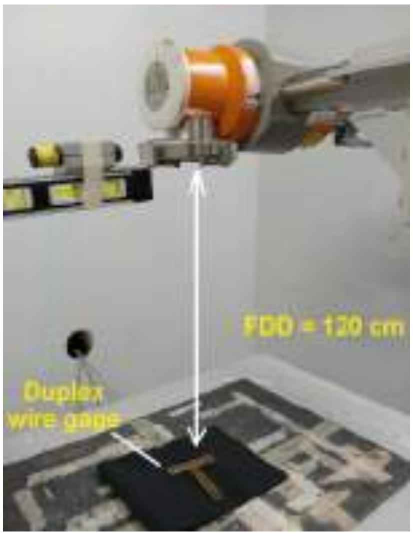

Figure 1. Basic spatial resolution, SRb measurement using phosphor imaging plate

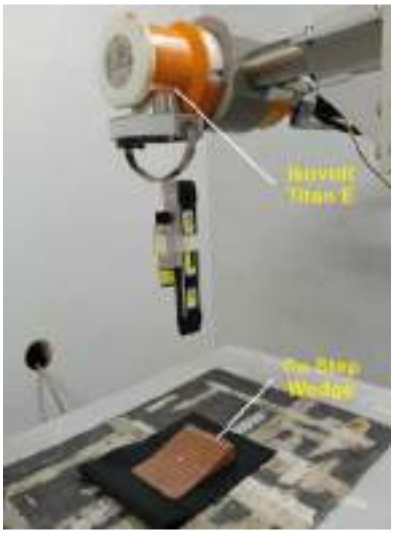

Figure 2. Experimental setup for SNR measurement using copper step wedge

RESULTS & DISCUSSION

Two horizontally and vertically images were analyzed to obtain the SR_b value using iSee! Software. The modulation transfer function (MTF) values were measured against each duplex wire thickness (Figure 3). The basic spatial resolution value at 20% was determined based on the MTF (%) graph against basic spatial resolution (µm) for both duplex wire images (Figure 4). The results showed that the SRb value for the computed radiography system with a white imaging plate was 112 µm.The gray value for each copper step wedge was determined with a region of interest (ROI) of 100 x 200, and a graph of normalized signal-to-noise ratio (SNR) against the gray value was plotted (Figure 5). The graph was found to be polynomial in nature, and the minimum gray value for testing class A (SNR = 70) was 10100 (Figure 6).)

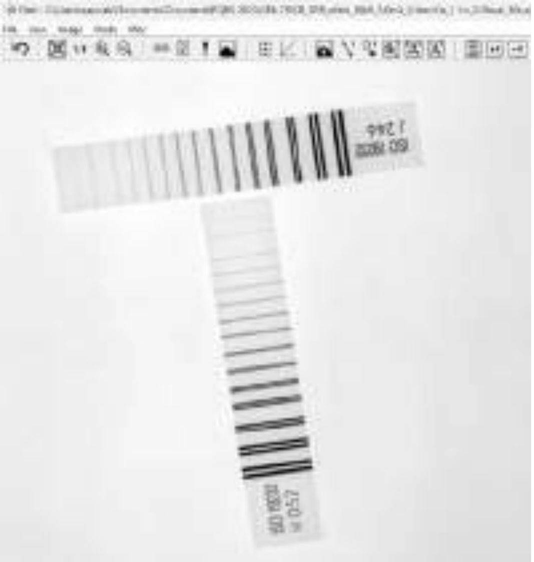

Figure 3. Duplex wire image for horizontal and vertical positions

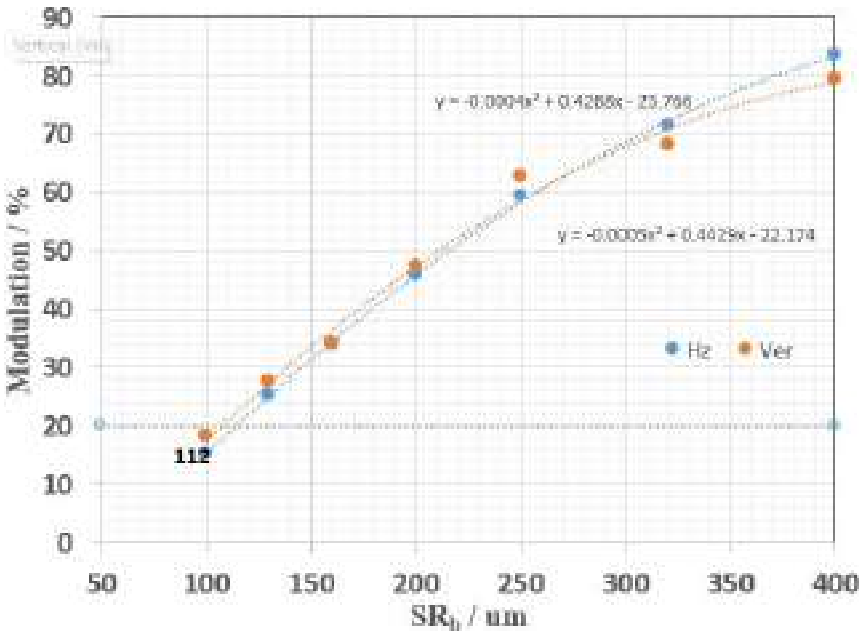

Figure 4. Determination of interpolated basic spatial resolution at 20% modulation depths of neighbored duplex wire elements

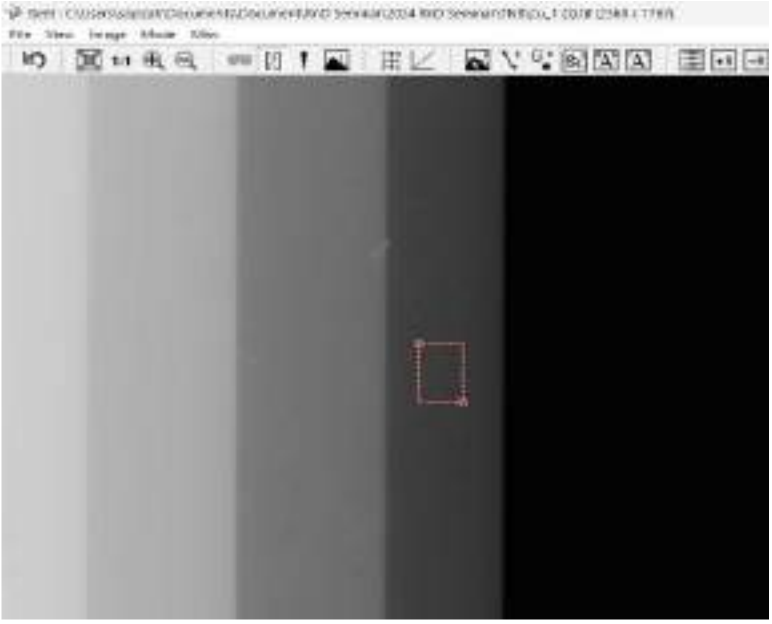

Figure 5. Gray value minimum determination using a copper step wedge.

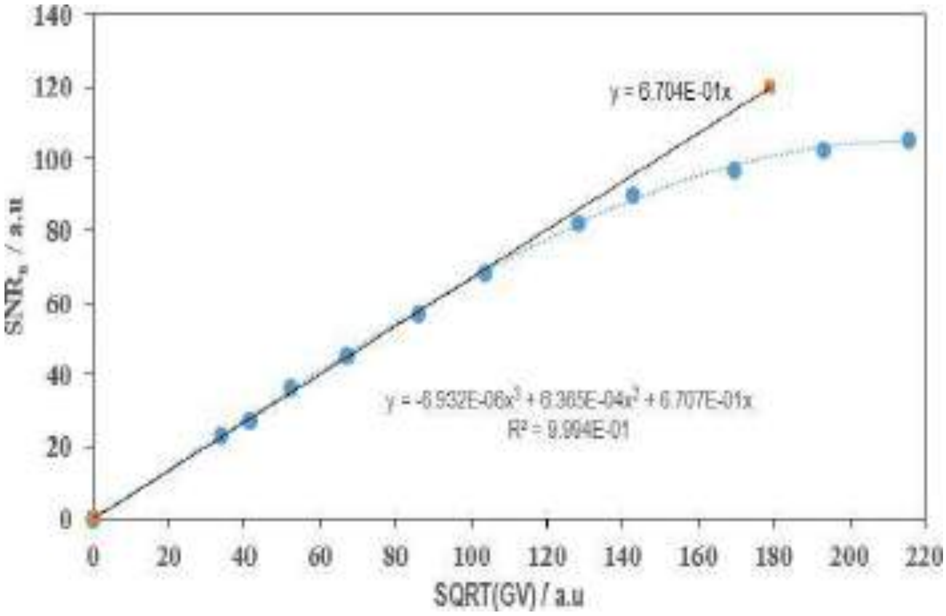

Figure 6. Graph of measured SNR versus the square root of gray value (16-bit system, SRb = 70 µm) for level I testing class determination

Therefore, this value was used as a reference to determine the exposure for each thickness and beam energy. The exposure for each thickness of steel with a specific beam energy was calculated using the following equation:

$$Exposure\ (mA.\min) = Current\ x\ time$$

Based on the minimum gray value obtained (~10100) and a focal spot-detector distance set at 700 mm with an SNR value of approximately 70 for testing class A, an exposure chart was developed (Figure 7a). The chart followed a similar trend to the exposure chart for film (Figure 7b), where thicker steel required higher energy to achieve the specified image sensitivity or quality. However, the exposure latitude for the phosphor imaging plate was lower, down to 0.1 mA.min, compared to film for the same thickness. This is because the imaging plate has a wide dynamic range that allows it to capture a broad spectrum of X-ray intensities, accommodating both very low and very high exposures in a single image. This reduces the risk of underexposure and overexposure, providing more consistent and reliable results. Additionally, the trend showed that at the same thickness of steel, the imaging plate required lower X-ray energy to achieve the required image quality.

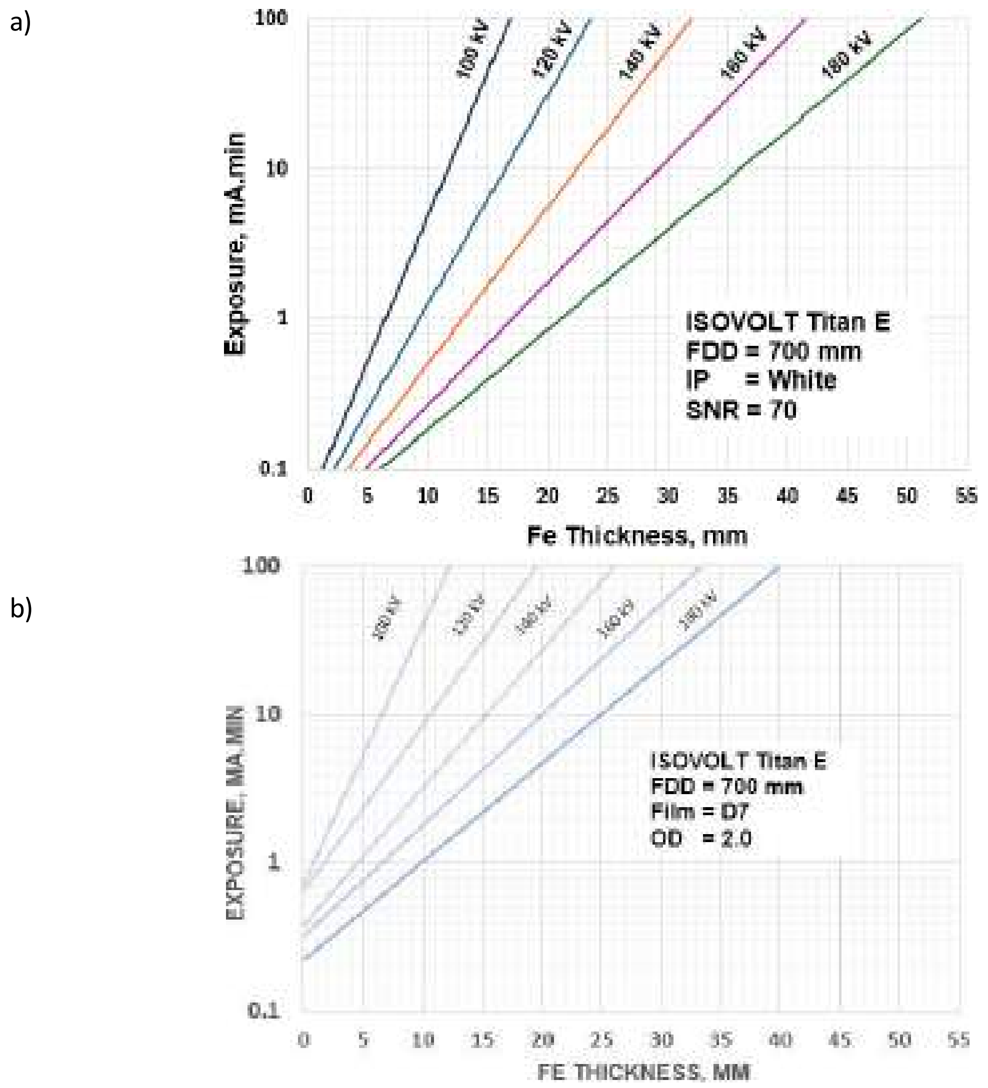

Figure 7. Exposure chart for (a) phosphor imaging plate and (b) film (replotted) for Isovolt Titan X-ray machine.

This chart has been validated by exposed a welded plate which has 10 mm nominal thickness (Figure 8). Radiographic image sensitivity for both developed exposure chart by imaging plate and film have been compared (Table 1). If both radiographic exposure have same radiographic arrangement, it is shown that using imaging plates have been reduced exposure time at about 80% from film exposure time. Furthermore, it was found that the exposure for each beam energy on the welded plate meets the required image quality, specifically SNR_n for testing class A (70) and the single wire that needs to be achieved (Table 1). This indicates that this computed radiography system only requires as low as 10100 a.u gray value to achieve the desired quality, and the developed exposure chart can be used to test structures of steel materials with different thicknesses. However, the exposure time for the imaging plate is shorter compared to film because the phosphor that reacts with X-rays is more sensitive, requiring only a low dose to form an image (Ou et al., 2021). This is because imaging plates are made of photostimulable phosphor, which is more sensitive to X-rays than industrial film and has a wider dynamic range. Therefore, less radiation is needed to produce a required image using an imaging plate, and it can capture a broader range of X-ray intensities in a single exposure. This reduces the need for longer exposure times to achieve the same image quality.

Figure 8. Radiograph image for welded plate using imaging plate for 140 kV beam energy

Table 1 : Compariosn of radigraphic image sensitivity for film and imaging plate for welded plate

10 mm Fe	**Required sensitivity**	**Film**	**naging Plate**
Exposure, mA.min	None	3.2	0.4
IQI (single wire : ISO)	W12	W12	W13
Duplex Wire	D8	None	D9
Signal-Noise Ratio (SNR)	70	None	101

CONCLUSION

In this study, an exposure chart was successfully developed for X-ray machine with phosphor imaging plates used in computed radiography systems. The results indicate that digital image generated from this X-ray machine and computed radiography system can achieve the required for class A testing (ISO17636-2). The developed exposure chart provides a valuable reference for NDT practitioners using computed radiography systems for inspecting steel components. The comparison with conventional film radiography demonstrates a significant reduction in exposure time, highlighting the efficiency and cost-effectiveness of computed radiography. Future work will focus on further optimizing the exposure chart for different materials and testing conditions to enhance the applicability of computed radiography in various NDT applications.

ACKNOWLEDGEMENT

NM-R&D-23-12; Development of X-ray Exposure Charts for Steel with phosphorus-based Imaging Plates. Thank you to Dr. Uwe Zscherpel, Senior Scientist at BAM (Bundesanstalt für Materialforschung und -prüfung) in Berlin, Germany, for advising on data analysis in this experiment.

REFERENCES

Korner, M., Weber, C. H., Wirth, S., Pfeifer, K.-J., Reiser, M. F., & Treitl, M. (2007). Advances in DigitalRadiography: Physical. *RadioGraphics*, *27*, 675–686.

Ou, X., Zhang, H., Lu, J., Hu, D., Yu, S., & Tang, S. (2021). Review Article RecentDevelopment in X-Ray Imaging Technology: Future and Challenges. *Research, 2021*.

Jurnal Sains Nuklear Malaysia, 2025, 37(No.1): 21 – 32
ISSN: 2232-0946

EFFECTS OF CHRONIC GAMMA IRRADIATION ON CASSAVA VAR. *UBI KUNING*

KESAN PENYINARAN GAMA KRONIK TERHADAP UBI KAYU VAR. *UBI KUNING*

Muniroh Md Saad[1*], Norazlina Noordin[1], Mustapha Akil[1], Shakinah Salleh[1], Norhafiz Talib[1], Zaki Hussain[1], Muhammad Abu Bakar[2], Muhammad Syamim Abdul Rahim[2] and Noor Shaireen Shahira Khalid[3]

[1]Agrotechnology and Biosciences Division,
Malaysian Nuclear Agency, Bangi, 43000 Kajang, Selangor
[2]Fakulti Sains Gunaan, UiTM Negeri Sembilan,
Cawangan Kuala Pilah, 72000, Kuala Pilah,Negeri Sembilan
[3]Department of Plant Science, Kulliyyah of Science, International Islamic
University Malaysia, 25200 Kuantan, Pahang Malaysia
*Correspondence author: muniroh@nm.gov.my

ABSTRACT

Cassava (Manihot esculenta Crantz) is one of the most essential carbohydrate crops worldwide, consumed by millions of populations in Africa, Asia, and Latin America (Parmar *et al.*., 2017). Cassava (Manihot esculenta Crantz) is one of the most essential carbohydrate crops worldwide, consumed by millions of populations in Africa, Asia, and Latin America (Parmar *et al.*., 2017). Cassava (Manihot esculenta Crantz) is one of the most essential carbohydrate crops worldwide, consumed by millions of populations in Africa, Asia, and Latin America (Parmar *et al.*., 2017). *Cassava, known scientifically as Manihot esculenta is one of the most essential carbohydrate crops worldwide, consumed by millions of populations in Africa, Asia, and Latin America. In Malaysia, Cassava produces various food items, including tapioca pearls, and cassava chips. Over the past two decades, advancements in mutation breeding techniques have significantly contributed to the genetic improvement of cassava, addressing challenges such as low yield, disease susceptibility, and poor nutritional content. Additionally, mutation breeding has facilitated the enhancement of root quality, including higher starch content and improved cooking properties. Cassava stem cuttings were exposed to various gamma irradiation dose rates (0.07 to 2.67 Gy/hour) over eight weeks. The results showed that survival rates remained high across most treatments, indicating cassava's resilience to radiation. However, plant height and bud formation were adversely affected by higher doses, with the highest cumulative dose (1709.49 Gy) resulting in the lowest plant height (30.4 cm) and reduced bud counts. Morphological changes, such as chlorophyll degradation and leaf abnormalities, were prevalent at higher doses. This suggests that while cassava can tolerate significant gamma irradiation, substantial doses impede growth and induce notable morphological mutations. Future research should focus on the growth of subsequent mutant generations to further understand the long-term impacts of chronic gamma irradiation on cassava.*

Keywords: Cassava var. Ubi Kuning, chronic gamma irradiation, mutation breeding, dose rate

ABSTRAK

Ubi kayu, yang dikenali secara saintifik sebagai Manihot esculenta, adalah salah satu tanaman karbohidrat yang paling penting di seluruh dunia, dimakan oleh berjuta-juta penduduk di Afrika, Asia, dan Amerika Latin. Di Malaysia, ubi kayu menghasilkan pelbagai produk makanan, termasuk bebola ubi kayu (tapioca pearls) dan kerepek ubi kayu. Sepanjang dua dekad yang lalu, kemajuan dalam teknik biakbaka mutasi telah menyumbang dengan ketara kepada peningkatan genetik ubi kayu, menangani cabaran seperti hasil yang rendah, kerentanan terhadap penyakit, dan kandungan nutrisi yang rendah. Selain itu, biakbaka mutasi juga telah membantu meningkatkan kualiti akar, termasuk kandungan kanji yang lebih tinggi dan sifat memasak yang lebih baik. Keratan batang ubi kayu telah didedahkan kepada pelbagai kadar dos sinaran gamma berbeza (0.07 hingga 2.67 Gy/jam) selama lapan minggu. Hasil kajian menunjukkan kadar kelangsungan hidup kekal tinggi dalam kebanyakan rawatan, menunjukkan ketahanan ubi kayu terhadap sinaran. Walau bagaimanapun, ketinggian tumbuhan dan pembentukan tunas terjejas oleh dos yang lebih tinggi, dengan dos kumulatif tertinggi (1709.49 Gy) menghasilkan ketinggian tumbuhan terendah (30.4 cm) dan bilangan tunas yang berkurang. Perubahan morfologi, seperti degradasi klorofil dan pembentukan daun yang tidak normah adalah lazim pada dos yang lebih tinggi. Ini menunjukkan bahawa walaupun ubi kayu dapat bertahan pada sinaran gamma yang tinggi, dos yang tinggi menghalang pertumbuhan dan menyebabkan mutasi morfologi yang ketara. Penyelidikan pada masa hadapan perlu fokus pada pertumbuhan generasi mutan seterusnya untuk memahami kesan jangka panjang sinaran gamma kronik pada ubi kayu.

Kata kunci: Ubi kayu var *Ubi Kuning*, Penyinaran gama kronik, Biakbaka mutasi, kadar dos

INTRODUCTION

Cassava (*Manihot esculanta*) also locally known as *ubi kayu* is a perennial woody shrub with edible roots, grown worldwide in tropical and subtropical climates (Amarullah *et al.* 2017; Oliveira and Miglioranza, 2014). Cassava is a vital local food source with a broad distribution and significant agroecological adaptability, making it the third most important tropical crop (Adiele *et al.* 2020; Neves *et al.* 2018; Hasibuan & Nazir, 2017). This versatile crop, a mesophyte, thrives in various environments, including fallow highlands, hill slopes, rice fields, and other underutilized highlands. This crop offers substantial development potential by providing essential calories and supporting food security for the growing population, particularly through local wisdom practices (Sulistiono *et al.* 2020; De Souza *et al.* 2017). Notably, cassava can grow in poor soils and still produce a reasonable yield, providing essential food security where other crops may fail (Siritunga *et al.* 2004). The ability to harvest cassava roots throughout the year ensures a reliable food supply for smallholder farmers and supplies raw materials for various processing industries (Rahman & Awerije, 2016).

According to the Food and Agriculture Organization of the United Nations (FAOSTAT, 2011), global cassava production exceeds 230 million metric tonnes annually. The leading producers include Nigeria, which yields approximately 37.5 million tonnes per year, Brazil with 24.5 million tonnes, and Thailand at 22.0 million tonnes. In Malaysia, the Department of Agriculture reported that 2023 around 2,815 hectares were dedicated to cassava cultivation, resulting in a production of about 46,156 metric tonnes (Department of Agriculture, 2023). Cassava has traditionally been used as a starch source in Malaysia (Tan & Khatijah, 2000). As understanding of the crop's potential expanded, the focus shifted to selecting cassava clones with lower cyanogen levels in the roots, making them suitable for direct consumption and food processing. Popular processed cassava foods include chips and crackers which are traditional snacks. Farmers currently cultivate two or three cassava varieties for chip production, including *Medan*, *Ubi Kuning*, and *Ubi Putih*.

Cultivation of cassava in Malaysia features a limited variety of both traditional and improved cultivars. While local traditional varieties have been cultivated for generations primarily for household consumption, they often face challenges such as susceptibility to pests, diseases, and generally low yields (Zainuddin *et al.* 2018). Improved varieties developed by the Malaysian Agricultural Research and Development Institute (MARDI), such as 'Sri Pontian' and 'Gajah', offer higher yields and better resistance to pests and diseases but are still limited in number compared to the extensive varietal diversity found in major cassava-growing regions like Africa and South America (Rahman *et al.* 2020). Despite these improvements, cassava farmers continue to struggle with common issues such as cassava mosaic disease (Patil and Fauquet, 2009), and root rot (Hohenfeld *et al.* 2022), which significantly impact production and profitability. Ongoing research and development efforts aim to enhance the existing cultivar pool and address these challenges to improve the overall productivity and sustainability of cassava cultivation in Malaysia.

Cassava varieties have a sterile genotype or produce highly heterozygous seeds with poor flowering which significantly hampers breeding efforts and genetic improvement of the crop. Sterile genotypes are unable to produce viable seeds, which restricts the generation of new genetic combinations through sexual reproduction. This leads to limited genetic diversity and reduces the potential for developing improved varieties with desirable traits such as increased yield, disease resistance, and environmental adaptability (Koundinya & Ajeesh 2023). Additionally, high heterozygosity and poor flowering complicate the breeding process, as it becomes challenging to select and stabilize traits over successive generations. The reliance on vegetative propagation in such cases, while effective for maintaining specific genotypes, limits the introduction of new genetic variations and slows down the overall breeding progress.

Mutation breeding has been a recognized method for creating new plant varieties with beneficial traits for a long time. Since the initial release of a mutant variety in the 1930s, the field has seen numerous notable achievements. A total of 3,308 new plant varieties have been developed globally through mutation breeding and have been registered with the International Atomic Energy Agency since 2019. Gamma irradiation has been widely used in plant breeding as a mutagenic agent to induce genetic diversity and improve traits like yield, disease resistance, and nutritional content (Ntsefong *et al.* 2023) However, the specific effects of chronic gamma irradiation on *Ubi Kuning*, particularly regarding its growth, development, and bud formation, are not well-documented. Previous research indicates that gamma irradiation can lead to cellular damage and morphological changes in plants (Wi *et al.* 2007), but the impacts on cassava specifically have not been extensively studied This lack of information limits the effective use of gamma irradiation for cassava improvement.

This study hypothesizes that chronic gamma irradiation will cause genetic mutations in *Ubi Kuning*, resulting in both positive and negative changes in its agronomic traits. It is expected that while certain doses of gamma irradiation may enhance traits such as disease resistance and nutritional content, they may also negatively impact growth parameters, including bud formation and shoot development. The procedure involved exposing cassava stem cutting to various dose rates of 0.66 Gy/hour (ring 2), 0.3 Gy/hour (Ring 3), 0.17 Gy/hour (Ring 4), 0.11 Gy/hour (Ring 5), 0.07 Gy/hour (Ring 6), and 0 Gy/hour (control) and observations were made on plant survival and morphological characteristics such as plant height, number of buds, and phenotypic/morphological variation. Therefore, this study was conducted to investigate the effects of chronic gamma irradiation on the growth and morphological changes in *Ubi Kuning.*

PROCEDURE

Plant Materials and preparation

Ubi Kuning stem cutting was obtained from Taman Kekal Pengeluaran Makanan (TKPM) Ulu Chuchoh, Sepang, Selangor. A total of 70 stem cuttings were used in this study. The stem cutting was chosen based on their diameter approximately five cm in diameter and was cut into 15 cm lengths each. The experiment was conducted using a completely randomized design (CRD) with seven treatments which are control, isodose ring 1,2,3,4,5, and 6 with 10 replicates for each treatment.

Chronic gamma irradiation exposure

A total of 60 *Ubi Kuning* stem cuttings were exposed to chronic gamma irradiation in the Gamma Greenhouse (GGH) facility in the Malaysian Nuclear Agency. The stem cuttings were placed in pots at 6 different dose rates ranging from 0.07 Gy/hour, 0.11 Gy/hour, 0.17 Gy/hour, 0.3 Gy/hour, 0.66 Gy/hour, and 2.67 Gy/hour. As for control treatment, a total of 10 stem cuttings were grown outside the gamma house under conditions very similar to those irradiated plants.

Data collection

Data on Plant Survival, plant height, number of buds, and morphological changes of the plants were observed during the experiment. Plants were taken out from GGH at Week 8 after planting and an accumulated dose of gamma irradiation for each treatment was collected at the end of the experiment.

Statistical Analysis

Analysis of variance was performed using Statistical Analysis System (SAS) version 9.2 to measure significant differences ($p \leq 0.05$) among characteristics data. The mean difference between doses was further tested using the least significant difference (LSD) method at 5%.

RESULTS AND DISCUSSION

Stem cuttings of *Ubi Kuning* were subjected to chronic gamma irradiation for 8 weeks (32 days) to study the plant's response to varying doses of gamma rays. Gamma rays, known for their high penetration ionizing radiation, are utilized as mutagens in plant mutation breeding. Chronic induced mutation from GGH can be used to irradiate different plant materials, including seedlings in pots, cuttings, calluses, somatic embryos, and suspension cell cultures (Nur Aziliana *et al.* 2015; Azhar, 2009). A previous study has reported that mutagenic treatment significantly affects plant survival rates and morphological traits (Harding and Mohamad, 2009; Mohamad *et al.* 2002). The data on cumulative dose is presented in Table 1.

Table 1: Cumulative dose

Isodose Ring	Dose Rate (Gy/hr)	Accumulative dose (Gy)
Control	0	0
1	2.67	1709.49
2	0.66	450.58
3	0.30	192.8
4	0.17	109.25
5	0.11	70.69
6	0.07	44.99

The survival rates of cassava under various treatment conditions are shown in Figure 1. The accumulated doses range from 0 to 1709.49 Gy, while the survival rate of *Ubi Kuning* at week 8 predominantly remains at 100%, except for a slight dip to 90% at an accumulated dose of 44.99 Gy. This suggests that the accumulated dose does not significantly impact the survival rate at week 8, maintaining a consistent level of 100% regardless of the dose, except for the minor deviation at the 44.99 Gy dose. This consistency indicates a potential threshold effect or resistance to change in response to increasing doses. Chronic irradiation differs significantly from acute gamma irradiation. Acute irradiation involves exposing samples to a high dose of radiation over a short period, whereas chronic gamma irradiation continuously exposes samples to low doses of radiation over an extended period. Theoretically, during chronic exposure, plant DNA undergoes continuous breakdown and repair, leading to mutations that help the plant survive (Mohd Zulmadi et al). This ongoing adaptation process might explain why the survival rate is not significantly affected by varying doses of gamma radiation.

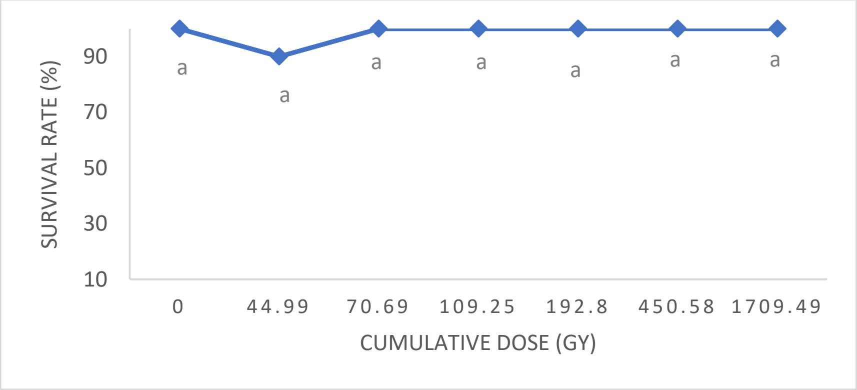

Figure 1: Effect of chronic gamma irradiation on the survival rate of *Ubi Kuning* at 8 weeks after planting

*Means with different letters between treatments indicate statistically significant differences at P≤0.05

Plant size and plant height have been reported to be affected by the dosage of mutagen received (Baadu *et al.* 2023). Figure 2 illustrates the impact of cumulative dose (Gy) on the height of *Ubi Kuning* plants measured at week 2 and week 8. Initially, at week 2, plant height increases with cumulative doses of 44.99 Gy, 70.69 Gy, and 109.25 Gy peaking at 12.25 cm. However, higher doses such as 192.8 Gy and 450.58 Gy result in significantly reduced heights of 8.9 cm and 6.1 cm, respectively compared to lower cumulated doses. At the extreme dose of 1709.49 Gy, the height further drops to 5.67 cm. Similarly, at week 8, the highest cumulative dose of 1709.49 resulted in the lowest plant height of 30.4 cm which is significantly different from other doses. The data suggest that very high doses of radiation are ultimately detrimental to the plant's height. Similarly, a significant reduction in plant height is also reported with higher doses of radiation in the *Chrysanthemum morifolium* variety ‘otome pink’ (Kumari *et al.* 2013). This radiation injury could be due to the inhibition of DNA synthesis or other physiological damage that not just appeared in plant height but could also be manifested in the form of plant survival and the number of plant organs (Nwachukwu, *et al.* 2009). Besides, Tiwari and Kumar (2011) also reported that many mutations can be lethal caused by the inhibition of cell division and induction of cell death. In some crops, lower plant height can be useful as it can withstand strong wind. Therefore, it does not mean that lower plant height cannot be selected for further screening.

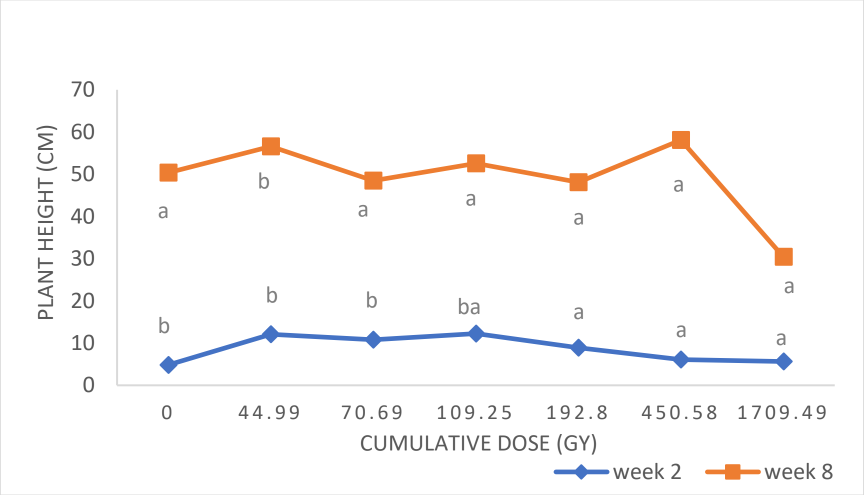

Figure 2: Effect of chronic gamma irradiation on plant height of *Ubi Kuning* at week 2 and week 8 after planting

*Means with different letters between treatments within the same week indicate statistically significant differences at P≤0.05

Figure 3 reveals the effect of cumulative doses (Gy) on the number of buds in *Ubi Kuning* plants over two time periods: week 2 and week 8. Initially, at week 2, the number of buds shows slight variations with cumulative doses, ranging from 3.0 to 3.6 buds. The control group (0 Gy) and the highest dose (1709.49 Gy) both exhibit 3.4 buds, indicating no immediate impact from extreme radiation levels. The highest bud count at week 2 is observed at 70.69 Gy with 3.6 buds, while the lowest is at 44.99 Gy with 3 buds with no significant difference between the dose rates. However, by week 8, there is a noticeable decline in the number of buds across all doses. The control group maintains the highest number of buds at 3.4, while all other groups show reduced bud counts, ranging from 2.4 to 2.7 buds. The highest dose of 1709.49 Gy results in a bud count of 2.5, similar to the mid-range doses of 192.8 Gy and 450.58 Gy. This data suggests that while radiation exposure may not drastically affect bud count in the short term, it leads to a consistent reduction in bud formation over an extended period. The number of buds can affect the number of leaves. Leaves are plant organs that perform photosynthesis, which produces carbohydrates for plants (Gardner *et al.* 2017). A previous study conducted by Hartati *et al.* 2021 showed that the low number of buds has a significant to very significant effect on plant height, stem diameter, and number of leaves. This is possible because as the number of buds increases, the nutrients produced from photosynthesis will be divided and distributed into many buds, resulting in decreased plant growth and yield.

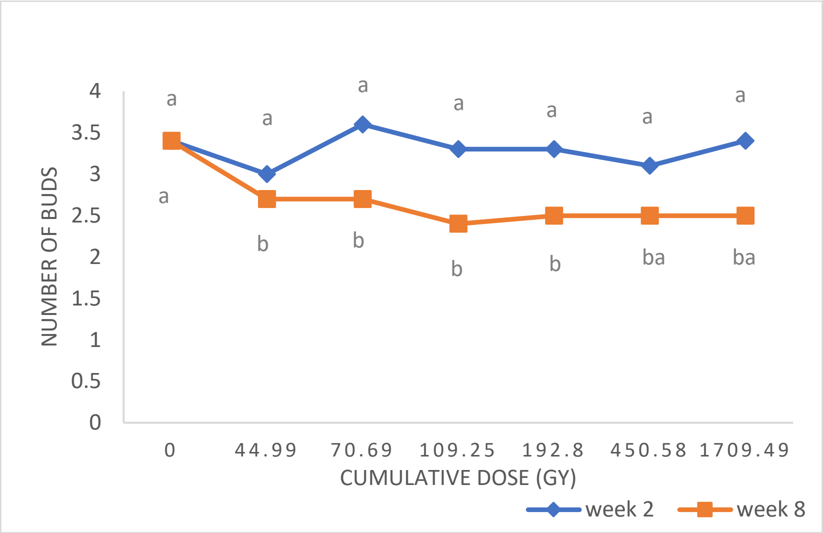

Figure 3: Effect of chronic gamma irradiation on the number of buds of *Ubi Kuning* at week 2 and week 8 after planting

*Means with different letters between treatments within the same week indicate statistically significant differences at P≤0.05

The study observed significant morphological changes in cassava plants exposed to chronic gamma radiation, with variations dependent on the dose level. Table 2 and Fig. 4a, 4b, and 4c show the morphological changes that can be observed at week 8 after planting for each isodose ring. At eight weeks after planting, control plants displayed normal coloration and typical leaf morphology with five lobes. In contrast, plants in all isodose rings exhibited chlorophyll degradation and various leaf abnormalities, including altered leaf shapes and variations in the number of lobes. Notably, plants in Isodose Rings 2, 4, and 5 showed additional symptoms of crinkled leaves. These findings suggest that chronic exposure to gamma radiation can disrupt normal plant development and physiology, leading to visible morphological changes. Changes in morphological characters after gamma radiation have been reported by many researchers in various types of plants including tea (Singh *et al.* 2023), maize (Marcu *et al.* 2013) chrysanthemum (Susila *et al.* 2019), and taro white (Fadli *et al.* 2018). The effect of gamma radiation on morphological character may be attributed to the stimulation of certain physiological processes or genetic responses within the plant (Riviello *et al.* 2022). Besides, chlorophyll mutation which can be seen on leaves, is a good indicator of the response to radiation and might be used as a parameter in accessing the frequencies of mutations at different doses (Azhar & Alsanulkhaliqin, 2014).

Table 2: Morphological changes observed at week 8 after planting

Treatment	Morphological Changes
Control	Normal Color with 5 number of lobes
Ring 1	Chlorophyll degradation Leaf abnormalities (Different shapes of leaves and different numbers of lobes)
Ring 2	Chlorophyll degradation Leaf abnormalities (Different shapes of leaves and different numbers of lobes) Crinkle leaves
Ring 3	Chlorophyll degradation Leaf abnormalities (Different shapes of leaves and different numbers of lobes)
Ring 4	Chlorophyll degradation Leaf abnormalities (Different shapes of leaves and different numbers of lobes) Crinkle leaves
Ring 5	Chlorophyll degradation Leaf abnormalities (Different shapes of leaves and different numbers of lobes) Crinkle leaves
Ring 6	Leaf abnormalities (Different shapes of leaves and different numbers of lobes)

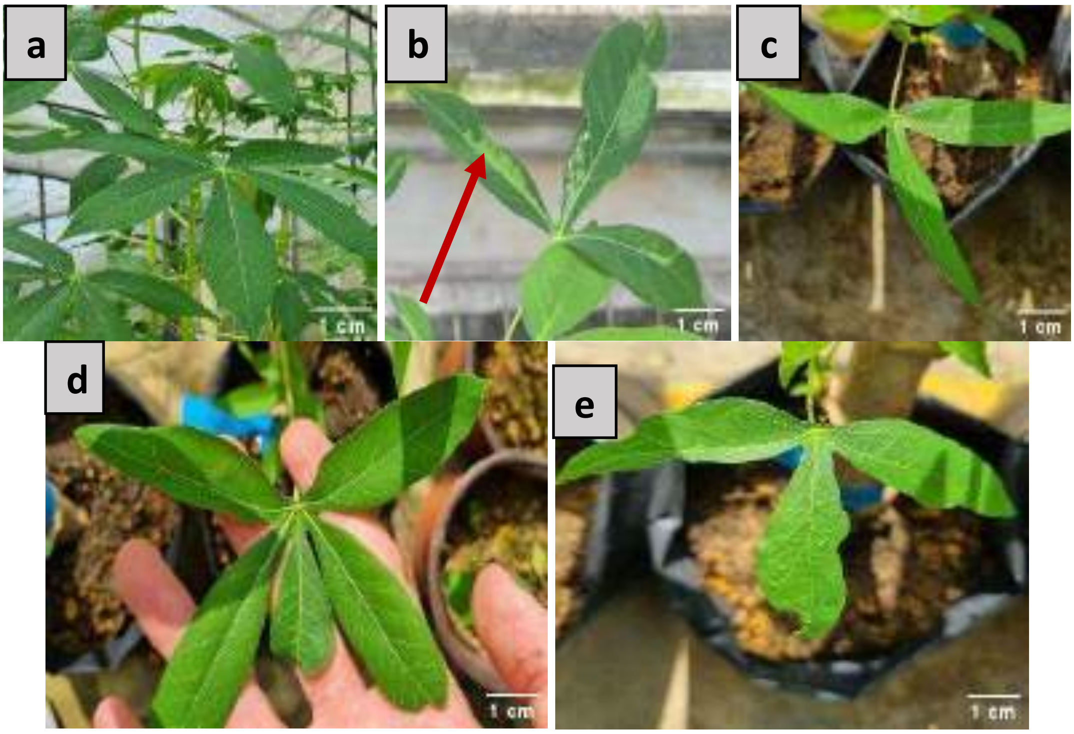

Figure 4: Leaves show (a) Normal color with 5 lobes (Control); (b) chlorophyll degradation; (c) Different numbers of lobes; (d) Different shapes of leaves; and (e) crinkled leaves

CONCLUSION

The study investigated the impact of chronic gamma irradiation on *Ubi Kuning* stem cuttings over 8 weeks, revealing that high doses of gamma rays can significantly alter plant morphology and growth. Survival rates remained consistently high across most treatment groups, indicating a robust tolerance to gamma irradiation. However, plant height and bud formation were adversely affected by higher radiation doses, with the highest cumulative dose (1709.49 Gy) resulting in the lowest plant height and reduced bud counts. Morphological changes, such as chlorophyll degradation and leaf abnormalities, were prevalent in irradiated plants, particularly at higher doses. These findings suggest that while *Ubi Kuning* can withstand substantial gamma radiation exposure, significant doses impede its growth and induce notable morphological mutations. This study can later be improved by observing the growth of the next mutant generation.

ACKNOWLEDGEMENT

The authors would like to thank the officers and staff from Taman Kekal Pengeluaran Makanan (TKPM) Ulu Chuchoh, Sepang, Selangor for the supply of *Ubi Kuning* stem cuttings. This acknowledgment also goes to all project members and the officers and staff of Agrotechnology & Biosciences Division, Malaysian Nuclear Agency.

REFERENCES

Adiele, J. G., Schut, A. G. T., van den Beuken, R. P. M., Ezui, K. S., Pypers, P., Ano, A. O., Egesi, C. N., & Giller, K. E. (2020). Towards closing cassava yield gap in West Africa: agronomic efficiency and storage root yield responses to NPK fertilizers. Field Crops Research, 253, 107820. H

Amarullah, Indradewa, D., Yudono, P., & Sunarminto, B. H. (2017). Correlation of growth parameters with yield of two cassava varieties. Ilmu Pertanian (Agricultural Science), 1(3), 100–104.

Azhar M., Rusli I., Sobri H. Gamma Greenhouse for Chronic Irradiation in Plant Mutation Breeding. Proceeding International Nuclear Conference, (2009), PWTC, Kuala Lumpur.

Azhar, M., & Ahsanulkhaliqin, A. W. (2014, February). Gamma greenhouse: a chronic facility for crops improvement and agrobiotechnology. In *AIP Conference Proceedings* (Vol. 1584, No. 1, pp. 32-37). American Institute of Physics.

Baadu, R., Chong, K. P., Gansau, J. A., Zin, M. R. M., & Dayou, J. (2023). A systematic review on physical mutagens in rice breeding in Southeast Asia. *PeerJ*, *11*, e15682

De Souza, A. P., Massenburg, L. N., Jaiswal, D., Cheng, S., Shekar, R., & Long, S. P. (2017). Rooting for cassava: insights into photosynthesis and associated physiology as a route to improve yield potential. New Phytologist, 213(1), 50–65. https://doi.org/10.1111/nph.14255

Department of Agriculture (2023). Crop Statistic Booklet- Food Crop Sub-Sector. Retrieved from Department of Agriculture website: https://www.doa.gov.my/doa/resources/aktiviti_sumber/sumber_awam/maklumat_pertanian/perangkaan_tanaman/booklet_statistik_tanaman_2023.pdf

Fadli, N., Syarif, Z., Satria, B., & Akhir, N. (2018). The effect of gamma Cobalt-60 ray irradiation on cultivar growth in taro white (Xhanthosoma sagittifolium L.). *International Journal of Environment, Agriculture and Biotechnology*, *3*(6), 268284.

FAOSTAT. (2011). FAOStat: Top Production—World (Total)—2009. Retrieved from FAO website: http:// faostat.fao.org/

Gardner, F. P., Pearce, R. B., & Mitchell, R. L. (2017). *Physiology of crop plants*. Scientific publishers.

Harding, S. S., & Mohamad, O. (2009). Radiosensitivity test on two varieties of Terengganu and Arab used in mutation breeding of roselle (Hibiscus sabdariffa L.). *African Journal of Plant Science*, *3*(8), 181-183.

Hartati, T. M., Roini, C., & Rodianawati, I. (2021). Growth response of local cassava to cutting models and the number of buds. *Caraka Tani: Journal of Sustainable Agriculture, 36(2), 379-391*

Hasibuan, S., & Nazir, N. (2017). The development strategy of sustainable bioethanol industry on iconic Sumba island, Eastern Indonesia. International Journal on Advanced Science, Engineering and Information Technology, 7(1), 276–283.

Hohenfeld, C. S., Passos, A. R., de Carvalho, H. W. L., de Oliveira, S. A. S., & de Oliveira, E. J. (2022). Genome-wide association study and selection for field resistance to cassava root rot disease and productive traits. Plos one, 17(6), e0270020.

Koundinya, A.V.V., Ajeesh, B.R. Flowering enhancement in cassava through gamma irradiation: a comparative study of gamma induced mutants *vis-a-vis* collected clones of cassava. *Plant Physiol. Rep.* **28**, 429–447 (2023). https://doi.org/10.1007/s40502-023-00736-6

Kumari, K., Dhatt, K. K., & Kapoor, M. A. N. I. S. H. (2013). Induced mutagenesis in Chrysanthemum morifolium variety 'Otome Pink'through gamma irradiation. *The Bioscan*, *8*(4), 1489-1492.

Marcu, D., Damian, G., Cosma, C., & Cristea, V. (2013). Gamma radiation effects on seed germination, growth and pigment content, and ESR study of induced free radicals in maize (Zea mays). *Journal of biological physics*, *39*, 625-634.

Mohamad, O., Nazir, B. M., Rahman, M. A., & Herman, S. (2002). Roselle: A new crop in Malaysia. *Bull. Genetics Soc. Malaysia*, *7*(1-2), 12-13.

Mohd Zulmadi, S., Faiz, A., Mustapha, A., Zaiton, A., Affrida, A. H., & Abdul Rahim, H. (2016). Effect of Chronic Gamma Irradiation on Kenaf (Hibiscus cannabinus. L) Variety V36. Research and Development Seminar 2016 (R&D Seminar 2016), Bangi (Malaysia).

Neves, R. J., Diniz, R. P., & Oliveira, E. J. (2018). Productive potential of cassava plants (Manihot esculenta Crantz) propagated by leaf buds. Anais Da Academia Brasileira de Ciências, 90(2), 1733–1747. http://dx.doi.org/ 10.1590/0001-3765201820170867

Ntsefong, G. N., Ernest, F. P., Kinsley, T. M., Hervé, Z. A., Noelle, M. H., & Martin, B. J. (2023). Gamma Ray Induced Mutagenesis for Crop Improvement: Applications, Advancements, and Challenges.

Nur Aziliana, M. Y., Shamsiah, A., Faiz, A. R. H., Rusli, I., Khairuddin, A. R., & Site Noorzuraini, A. R. (2015). The effect of chronic gamma irradiation on malaysia upland rice (Oryza sativa) kuku belang. *Australian Journal of Basic and Applied Science*, *9*(31), 1-6.

Nwachukwu, E. C., Mbanaso, E. N. A., & Nwosu, K. I. (2009). The development of new genotypes of the white yam by mutation induction using yam mini-tubers. *Induced Plant Mutations in the Genomics Era. Rome: FAO*, 309-312.

Oliveira, E. C., & Miglioranza, E. (2014). Stomatal density in six genotypes of cassava. International Journal of Engineering Science and Innovative Technology (IJESIT), 3(3), 205–208. Retrieved from http://www.ijesit.com/Volume%203/Issue%203/IJESIT201403 _40.pd

Patil, B. L., & Fauquet, C. M. (2009). Cassava mosaic geminiviruses: actual knowledge and perspectives. Molecular plant pathology, 10(5), 685-701.

Rahman, S., & Awerije, B. O. (2016). Exploring the potential of cassava in promoting agricultural growth in Nigeria. Journal of Agriculture and Rural Development in the Tropics and Subtropics (JARTS), 117(1), 149–163. Retrieved from https://www.jarts.info/index.php/jarts/article/view/2016050350 174

Rahman, N., Supatmi, S., Fitriani, H., & Hartati, N. S. (2020). Morphological Variation and Beta Carotene Contents of Several Clones of Ubi Kuning Cassava Genotype Derived from Irradiated Shoot in vitro. Jurnal Ilmu Dasar, 21(2), 73-80.

Singh, S. K., Borthakur, D., Tamuly, A., Manjaya, J. G., Patel, P. K., Gogoi, B., Sabhapandit, S., Neog, N. J., & Barooah, A. K. (2023). Assessment of gamma radiation through agro-morphological characters in Camellia sinensis L.(O.) Kuntze. International Journal of Radiation Biology, 99(5), 866-874.

Siritunga, D., Arias-Garzon, D., White, W. and Sayre, R.T. (2004). Over-expression of hydroxynitrile lyase in transgenic cassava roots accelerates cyanogenesis and food detoxification. Plant Biotechnology Journal, 2(1), 37-43. https://doi.org/10.1046/j.1467-7652.2003.00047.

Sulistiono, W., Hartanto, S., & Brahmantiyo, B. (2020). Respons beberapa varietas ubi kayu terhadap pemupukan NPK pada tanah Latosol di Maluku Utara. Buletin Palawija, 18(1), 43–51. http://dx.doi.org/10.21082/bulpa.v18n 1.2020.p43-51

Susila, E., Susilowati, A., & Yunus, A. (2019). The morphological diversity of Chrysanthemum resulted from gamma ray irradiation. *Biodiversitas Journal of Biological Diversity*, *20*(2), 463-467.

Tan, S.L. and I. Khatijah. 2000. Present situation and future potential of cassava in Malaysia. Paper presented at the 6th Asian Cassava Workshop, Ho Chi Minh City, Vietnam, Feb 21- 25, 2000.

Tiwari, A. K., & Kumar, V. (2011). Gamma-rays induced morphological changes in pot marigold (Calendula officinalis). *Progressive Agriculture*, *11*(1), 99-102.

Wi, S. G., Chung, B. Y., Kim, J. S., Kim, J. H., Baek, M. H., Lee, J. W., & Kim, Y. S. (2007). Effects of gamma irradiation on morphological changes and biological responses in plants. Micron, 38(6), 553-564.

Zainuddin, I. M., Fathoni, A., Sudarmonowati, E., Beeching, J. R., Gruissem, W., & Vanderschuren, H. (2018). Cassava post-harvest physiological deterioration: From triggers to symptoms. Postharvest Biology and Technology, 142, 115-123.

Jurnal Sains Nuklear Malaysia, 2025, 37(No.1): 33 – 49
ISSN: 2232-0946

PREDICTION OF RTP FUEL SOURCE TERM AND DECAY HEAT IN SURROUNDING MATERIALS

Mohamad Hairie Rabir*, Mark Dennis Usang, Muhammad Khairul Ariff Mustafa, Julia Abdul Karim and Mohamad Amirudin Mohamad Rosli

Reactor Technology Centre, Malaysian Nuclear Agency
*Corresponding author: m_hairie@nm.gov.my

ABSTRACT

This study aims to predict the source term and decay heat of highly burned-up fuel from the RTP TRIGA reactor, a critical factor for ensuring safe handling and disposal. Data on the reactor's operational history and accumulated burnup were collected and analyzed. Burnup calculations were carried out using the TRIGLAV code, while nuclide inventory simulations were performed with the MCNPX code. The decay heat was also evaluated using MCNPX. The gamma radiation strength for a core case and the decay heat resulting from energy deposition within the spent fuel pool were assessed. Additionally, the conservative maximum source term for a single fuel element was determined, highlighting the contribution of gamma radiation from radionuclides to decay heat in surrounding materials. This study provides vital data on the source term and decay heat, supporting the safe management of spent fuel from the TRIGA reactor.

Keywords: Decay Heat, TRIGA Fuel, Sourceterm, MCNPX, TRIGLAV

INTRODUCTION

PUSPATI TRIGA Reactor

The Malaysian PUSPATI TRIGA Reactor (RTP), located at the Malaysian Nuclear Agency, achieved its first criticality on 28 June 1982 and remains the nation's only research reactor. Operating at a maximum thermal power of 1 MW, the reactor generates a neutron flux of up to 10^{13} $n \cdot cm^{-2} \cdot s^{-1}$, supporting applications in neutron activation analysis, isotope production, and reactor physics experiments. Its core utilizes U-ZrH fuel, known for its inherent safety characteristics, with a mixed configuration of three types of fuel elements, each with varying uranium weight percentages to support different operational and research needs. Since its initial operation, the RTP core has undergone 16 reshufflings to address fuel depletion and burnup (Rabir et al., 2022).

The latest core configuration, Core-16, is depicted in Figure 1. It features an annular core surrounded by a graphite reflector and cooled via natural convection. The core's seven concentric rings of fuel elements are interspersed with water, serving as both coolant and moderator. Core-16 comprises fuel elements of 8.5 wt.%, 12 wt.%, and 20 wt.% UZrH1.6 with 20% U-235 enrichment, along with four control rods, graphite elements, and a central thimble. Fuel dimensions are detailed in Figure 2. RTP employs four boron carbide control rods, three of which are fuel follower types, containing 8.5 wt.% UZrH1.6 and a B4C absorber above the fuel section, while the fourth is an air follower (Rabir et al., 2022).

The TRIGA reactor, with an estimated operational lifespan of 50 to 60 years, has seen the PUSPATI TRIGA Reactor already surpass 40 years of service (IAEA, 2016). As RTP approaches the end of its operational life, the development of a decommissioning plan is actively underway to ensure a structured and safe process. Key future decommissioning activities will include facility dismantling and spent fuel management, both of which require meticulous planning and execution. Initial preparatory efforts for spent fuel management are already in progress, focusing on the design and fabrication of a fuel transfer cask (FTC) and the design, construction, and commissioning of a spent fuel pool (SFP) facility. Additionally, the implementation of an ageing management program is critical to maintain safety and ensure operational reliability throughout the reactor's remaining years (IAEA, 2014).

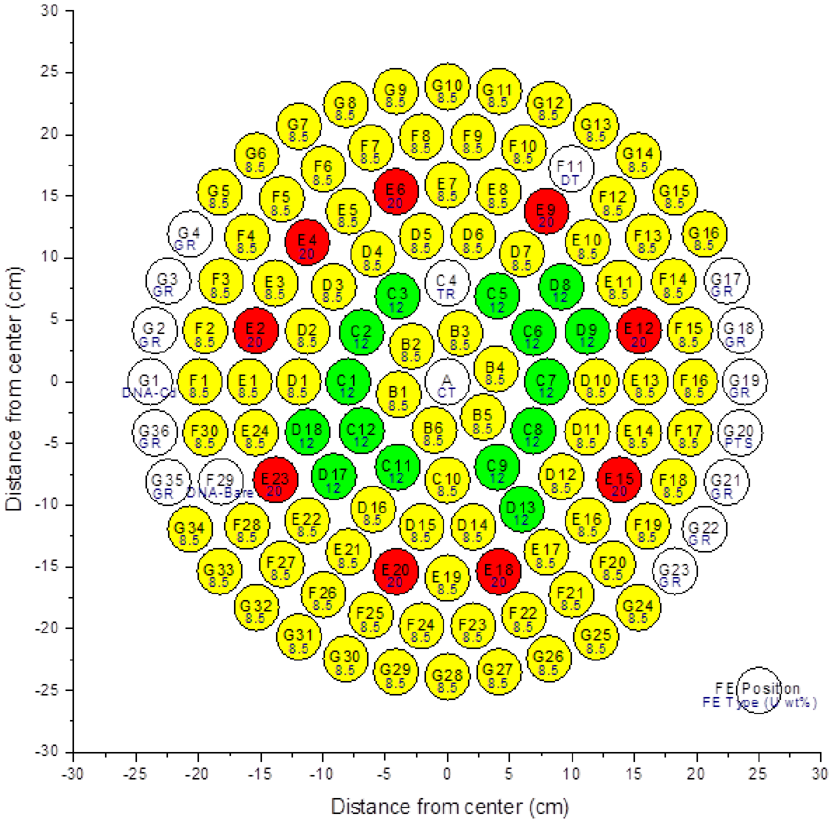

Figure 1: RTP's 16th core configuration featuring three types of fuel elements: 8.5 U wt. % (yellow), 12 U wt. % (green), and 20 U wt. % (red).

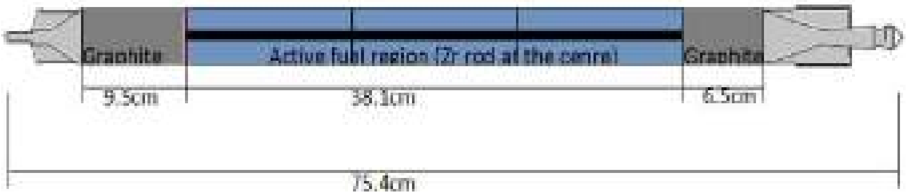

Figure 2: RTP fuel dimension

Importance of the subject

A comprehensive plan for managing highly burned-up research reactor fuel is critical to ensuring safety and compliance with regulatory requirements. The effective handling of such fuel demands meticulous preparation and the systematic collection of all relevant data. This includes detailed characterization of the fuel, focusing on parameters such as burnup, radionuclide inventory, and source-term determination. Understanding the source term is particularly important as it directly influences radiation safety measures, including shielding design and occupational exposure limits. Additionally, accurate source-term data enable precise modeling of radiological hazards during transport, storage, and eventual disposal, ensuring the protection of workers, the public, and the environment (El Maliki El Hlaibi et al., 2023).

Another crucial aspect to consider is the potential decay heat generated by the spent fuel and its impact on the surrounding structures within the storage facility. Decay heat can lead to thermal stress and material degradation, affecting the structural integrity of storage systems over time. Therefore, thermal analysis of the storage environment, including the interaction between the fuel and its containment, must be performed. This ensures that the facility design accommodates both immediate and long-term thermal loads, maintaining safe conditions throughout the storage period. By addressing these factors, the plan will provide a robust framework for the safe and sustainable management of highly burned-up research reactor fuel (Rochman et al., 2024).

Aim of study

The heat generated by the radioactive decay of fission products, known as radiation decay heat, is a critical factor to consider after a reactor shutdown. To support ongoing efforts in characterizing TRIGA reactor fuel for future handling procedure, this study focuses on evaluating decay heat with the following objectives: (1) To determine the radiation source term for the entire current RTP fuel inventory at its current burnup levels and for a single fuel element under extreme theoretical burnup conditions, (2) To identify the maximum radiation source term of an individual TRIGA fuel element, (3) To assess energy deposition due to decay heat within the SFP and the FTC.

The primary concern regarding decay heat lies in its long-term impact on structural integrity rather than immediate effects leading to incidents or accidents. In emergency scenarios, such as an accidental loss of coolant from the reactor pool, natural convection of air effectively removes fission product decay heat. This mechanism is sufficient to maintain fuel temperatures below critical levels, provided decay heat production is minimal or sufficient time has elapsed since reactor shutdown. Analytical results indicate that standard TRIGA fuel can tolerate temperatures up to 900°C without compromising cladding integrity. Furthermore, under coolant loss conditions, these thresholds are not surpassed if the thermal power per fuel element remains below 21 kW, ensuring structural safety (IAEA, n.d.).

METHODS

SFP design

As part of the RTP facility, SFP and FTC were constructed to support the future handling of spent or irradiated fuel. Concrete plays a critical role as a shielding material within the fuel pit facility and as shielding blocks. These materials were modeled and analyzed using MCNPX simulations to account for the decay heat generated by gamma radiation emitted from the fuel. The basic design of the SFP is illustrated in Figure 3. It consists of three fuel racks submerged in water at a depth of 4.5 meters and a width of 4.5 meters. All irradiated fuel is assumed to be loaded within these racks. In the MCNPX model, the SFP is divided into seven sections labeled A, B, C, D, E, F, G, along with a stainless-steel lining. Each section is assigned increasing neutron importance values (indicated by color coding) to enhance statistical accuracy as gamma radiation propagates farther from the source (fuel racks). Figure 4 displays the neutron importance values on the left and the corresponding section volumes on the right.

FTC design

The design of the Fuel Transfer Cask (FTC), shown in Figure 5, represents a standard configuration commonly utilized in TRIGA reactor facilities. The MCNPX model incorporates detailed material specifications, such as lead filling and a stainless-steel frame/wall, along with precise dimensional data. However, for the F6 tally, only the volume within the axial height of the fuel is considered. The FTC's radial model is segmented into radial sections (see Figure 6), following a similar methodology to the neutron importance assignments used for the SFP. This segmentation, based on varying neutron importance, enhances simulation accuracy. Additionally, dividing the model into separate cell volumes simplifies the application of cell tallies, such as F6 or F4, during MCNPX simulations.

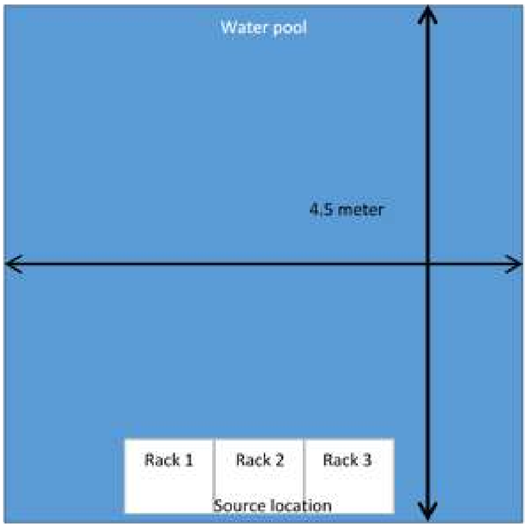

Figure 3: Basic design of SFP

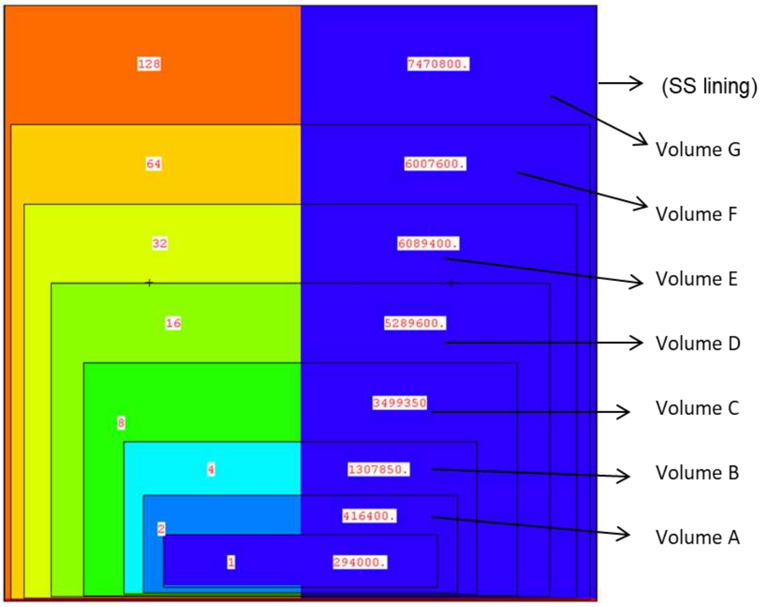

Figure 4: Sections in MCNPX model of the SFP

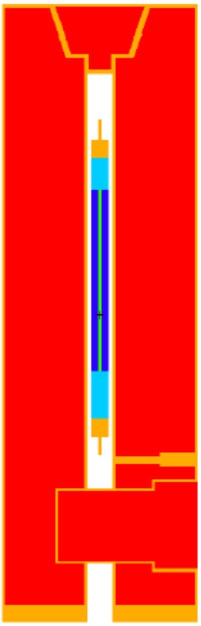

Figure 5: MCNPX model of TRIGA fuel inside FTC

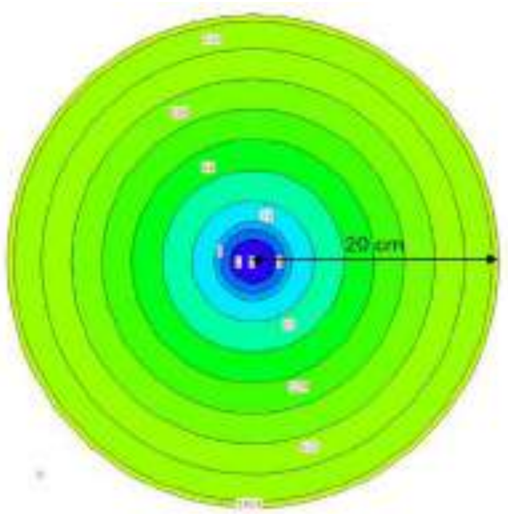

Figure 6: Radial sections in MCNPX model of the FTC

Simulation flow

The simulation process (see Figure 7) to estimate decay heat in the SFP begins with analyzing reactor operation history data, which provides key information on power levels and operating periods, forming the baseline for TRIGLAV calculations. From this, the core burnup is determined, and the burnup for individual fuel elements is obtained (Rabir et al., 2022). Using the calculated burnup, the radionuclide inventory is assessed via MCNPX's CINDER90 code, providing detailed information on the types and quantities of radioactive isotopes present in the spent fuel (Pelowitz, 2011) . Subsequently, the gamma radiation intensity and energy spectra emitted by the radionuclides in the fuel elements are evaluated. This data is then used in a separate MCNPX simulation to estimate the decay heat deposition within the SFP.

Additionally, a separate case was simulated to assess a single fuel element with the highest uranium content, conservatively assuming a burnup of up to 50%. The resulting radionuclide inventory and gamma radiation characteristics were determined before calculating its decay heat. To broaden the study's scope, simulations were also conducted to evaluate decay heat in the FTC, traditionally made of lead. Alternative materials, including normal concrete and high-density concrete, were also analyzed in separate simulations to explore their viability in decay heat management.

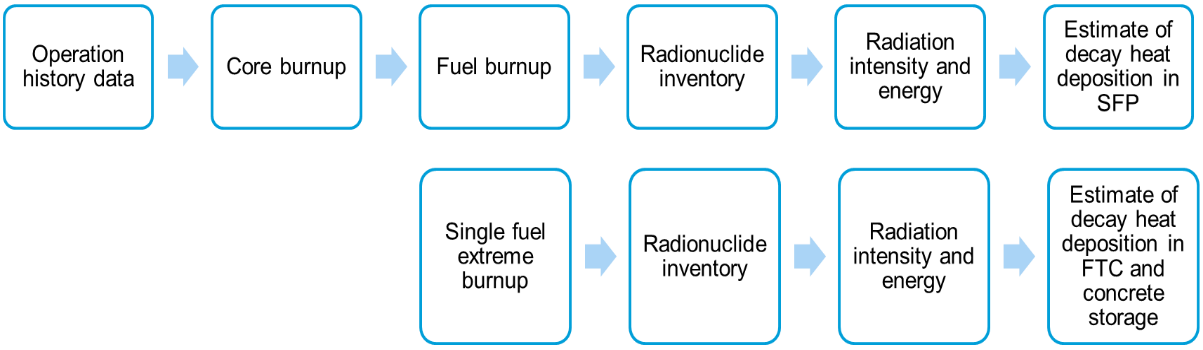

Figure 7: Simulation process flow for decay heat in the SFP (top) and the FTC with concrete shielding (bottom).

Operational data collection

Figure 8 illustrates the accumulation of burnup (measured in MWdays) over time, starting in February 1982 and projected into the 2030s. As of now, the RTP has accumulated approximately 800 to 850 MWdays of burnup, based on data retrieved from the RTP operational database. This burnup data is essential for TRIGLAV calculations, which provide a detailed record of fuel usage, and for MCNPX simulations, which predict the fission product inventory over the reactor's operational lifetime.

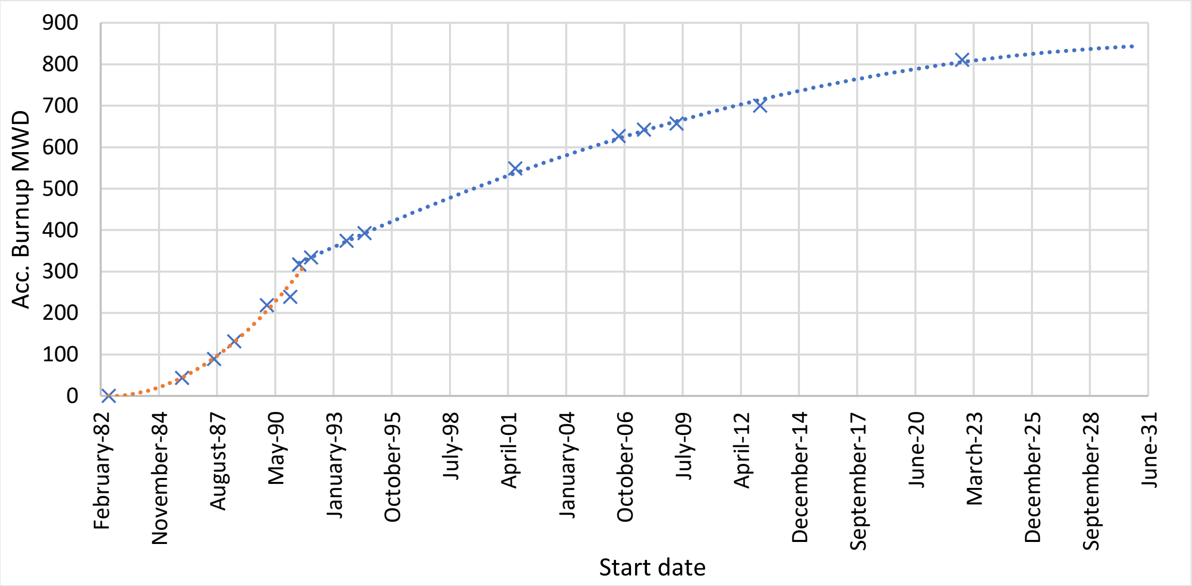

Figure 8: RTP accumulated total burnup

TRIGLAV burnup calculation

TRIGLAV is a deterministic code based on the diffusion approximation of the transport equation that employs the WIMSD program to calculate an averaged unit cell cross section. Core and individual fuel element burnup will be determined using the TRIGAV code (Rabir et al., 2022). As depicted in Figure 9, each fuel element (FE) will have a distinct burnup value due to its initial composition, loading history, and location within the core (Pungerčič et al., 2020).

TRIGLAV was selected for burnup calculations due to its validation for TRIGA reactors, computational efficiency, compatibility with RTP's operational data, and its successful integration with MCNPX for nuclide inventory and decay heat simulations. Compared to Monte Carlo-based alternatives like SERPENT or MCNPX-BURN, TRIGLAV offers a faster and deterministic approach, making it suitable for large-scale parametric studies.

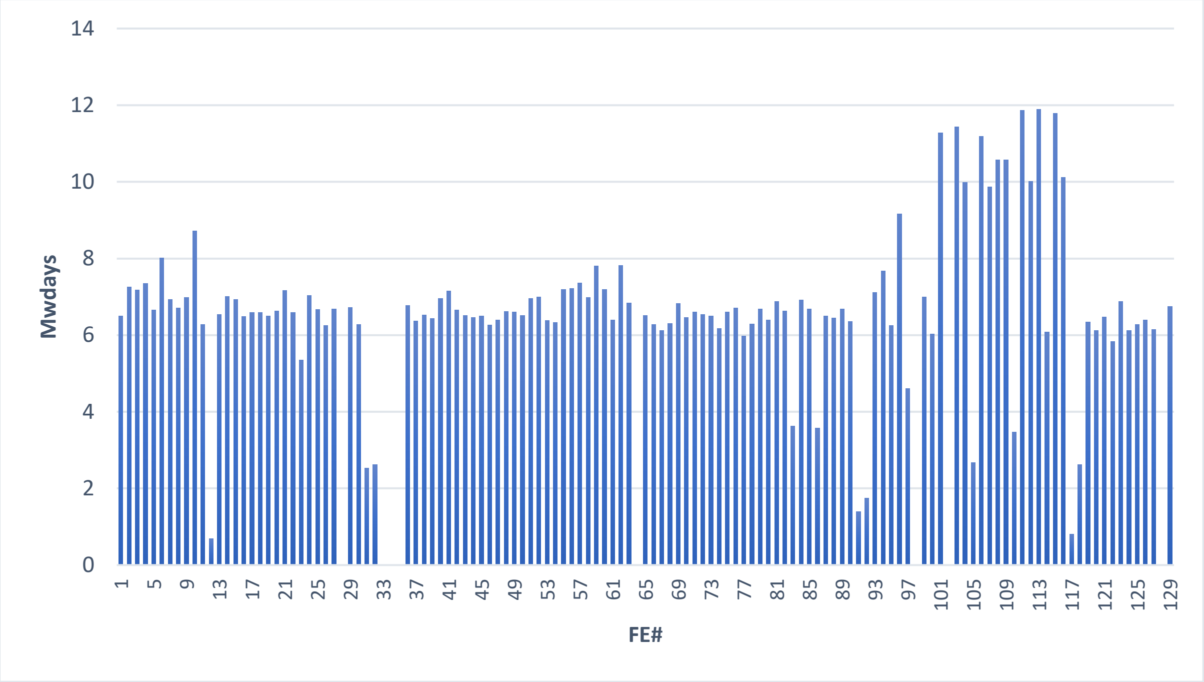

Figure 9: RTP individual fuel burnup values in MWdays, with each fuel element assigned a unit number up to #129.

Burnup and nuclide inventory simulation using MCNPX

The MCNPX code will be utilized to generate the nuclide inventory of each FE based on the burnup calculation from the TRIGLAV code. In the end, MCNPX fuel and core model of RTP Core-16 is developed using the nuclide inventories obtained previously. TRIGLAV generates burnup data for each RTP fuel element in units of MWdays, and this value is used as input in the MCNPX model. MCNPX performs burnup simulations and calculates the formation of actinides, fission products, and activation products in the RTP fuel for each different burnup value. This simulation is carried out using the 'BURN' card, where CINDER90 computes depletion, decay, and tracks all radionuclide changes in the model. Subsequently, the radiation emitted by radionuclides in the fuel is determined based on available published nuclide databases. This study focuses exclusively on gamma radiation to evaluate decay heat impacting materials surrounding the fuel. For scenarios involving extreme single-fuel burnup, MCNPX is directly utilized to simulate the theoretical burning of the selected fuel type until 50% of its fissile material is depleted, bypassing the use of MWdays as a reference.

After determining the gamma energy distribution and intensity, the F6 tally was employed to model decay heat. The F6 tally in MCNP calculates energy deposition within a material, which helps assess the dose or heating resulting from radiation interactions. It measures the energy deposited per unit mass (e.g., MeV/g) due to particle interactions within a specified cell. The tally output, measured in units of MeV/g, can then be directly converted into Watt-seconds (W·s) by applying the appropriate conversion factor. This energy value is scaled using both the mass of the fuel meat and the actual gamma intensity from the fuel, which was determined earlier in the analysis [7].

RESULTS AND DISCUSSION

Radionuclide inventory

MCNPX generates detailed radionuclide inventories, including buildup and decay following the cessation of fission, for each of the irradiated (from the total 129) fuel elements. Figures 10 and 11 present the actinide and non-actinide fission product inventories for a representative fuel element (FE#109). The inventories for other fuel elements exhibit similar trends, with variations in radionuclide magnitudes corresponding to differences in burnup values.

The actinides with the highest mass, aside from U-238 and U-235, include U-236 and Pu-239, as illustrated in Figure 10. In TRIGA fuel, the most significant actinides are U-236 and Pu-239. U-236 is primarily formed when U-235 captures a neutron without undergoing fission, although most of the U-236 nuclei eventually undergo fission to achieve stability. In contrast, Pu-239 is generated through the transmutation of U-238. This process involves neutron absorption by U-238, converting it to U-239, which then undergoes beta decay to form Np-239, followed by further beta decay to produce Pu-239.

The majority of the gamma radiation in spent fuel originates from the radioactive decay of these fission products, which include elements like Cs-137. The fission products inventory, as shown in Figure 11, includes several elements at the top, notably the isotopes of Xenon, Cesium, Neodymium, Promethium, Technetium, and Samarium. The selected nuclides are ranked based on their contribution to decay heat, which is a critical factor in post-irradiation fuel management. Cs-137 and Cs-134 are the dominant sources of medium- and short-term decay heat, respectively, due to their high fission yields and beta decay energies. Pm-147 also contributes significantly to early decay heat, particularly within the first few years after shutdown. I-127 and its decay product Xe-135 play a vital role in the initial hours to days, affecting both decay heat and reactivity control. While Sm-149 is not a major heat emitter, it is included due to its buildup from short-lived precursors and its strong neutron absorption that indirectly influences reactor cooldown behavior. Tc-99, though contributing minimally to decay heat, is considered for its long-term radiological impact and relevance in waste disposal. This ranking supports a more focused assessment of thermal behavior in spent fuel systems.

Gamma energy spectrum and intensity

MCNPX provides radionuclide data, including mass and activity in curies, which can be used to estimate radiation intensity. The energy and yield of each emitted radiation are derived from established published databases. Using this approach, all gamma energies and their intensities for the burned fuel elements were compiled, as summarized in Table 1.

This data can be evaluated for any specified decay time. For this analysis, a decay period of one year was chosen as a conservative baseline, aligning with the common practice of cooling and decaying fuel for at least 10 years before transfer to the SFP during the decommissioning process.

After one year of decay, specific gamma energies dominate the decay heat contribution. Among these, the 661.66 keV gamma radiation is the most significant, accounting for 8.13×10^{13} gamma/s or 61.1% of the total emitted gamma radiation. For the single fuel case, a similar trend was observed in the radionuclide species and gamma energy distribution, albeit with significantly lower magnitudes. This is illustrated in Figures 12 and 13. It is important to note that gamma energies with fractions of 1 × 10^{-9} or lower were excluded from the analysis across all cases.

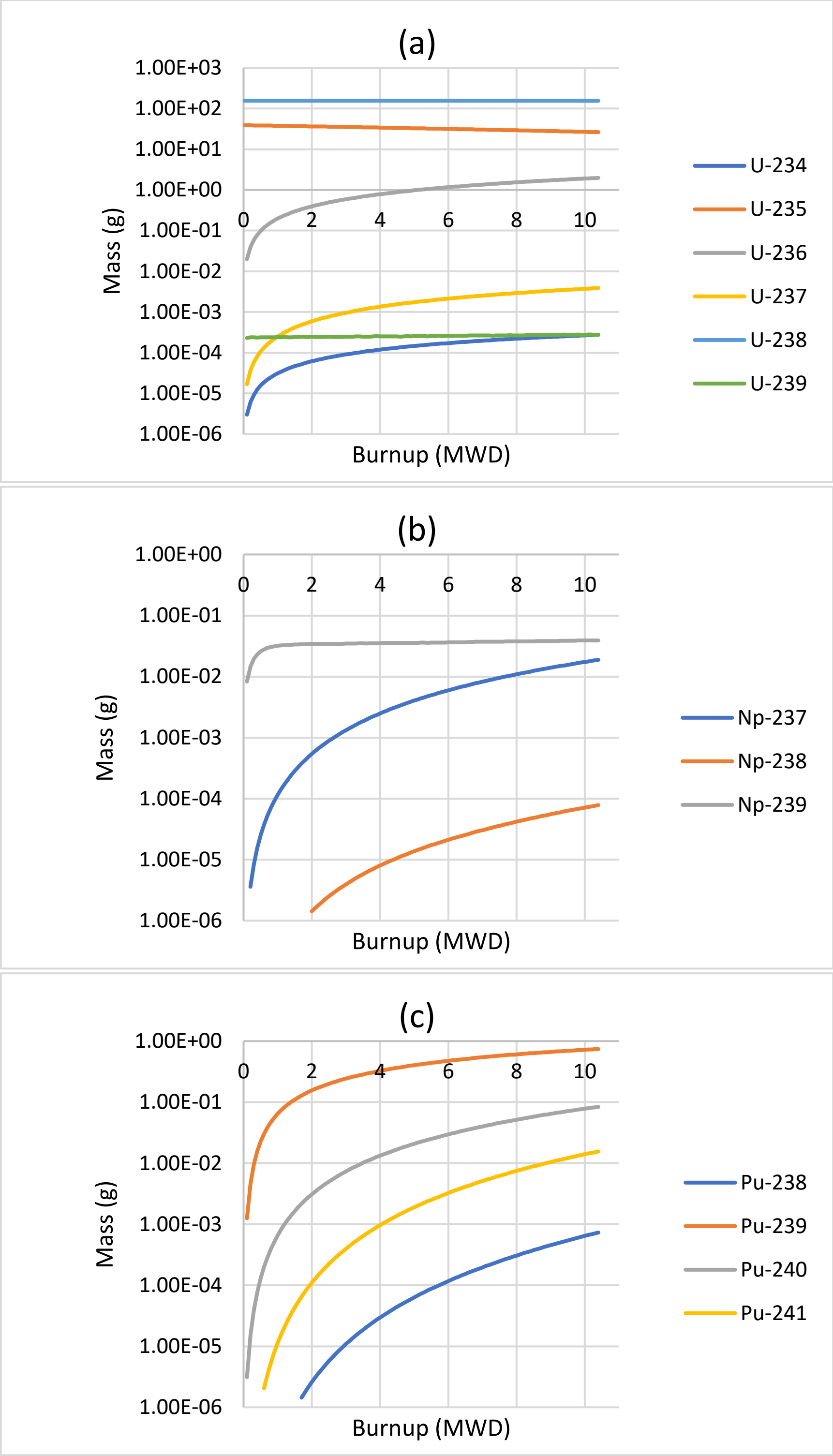

Figure 10: Isotopic inventory of major actinides in fuel element #109, showing Uranium (a), Neptunium (b), and Plutonium (c) isotopes.

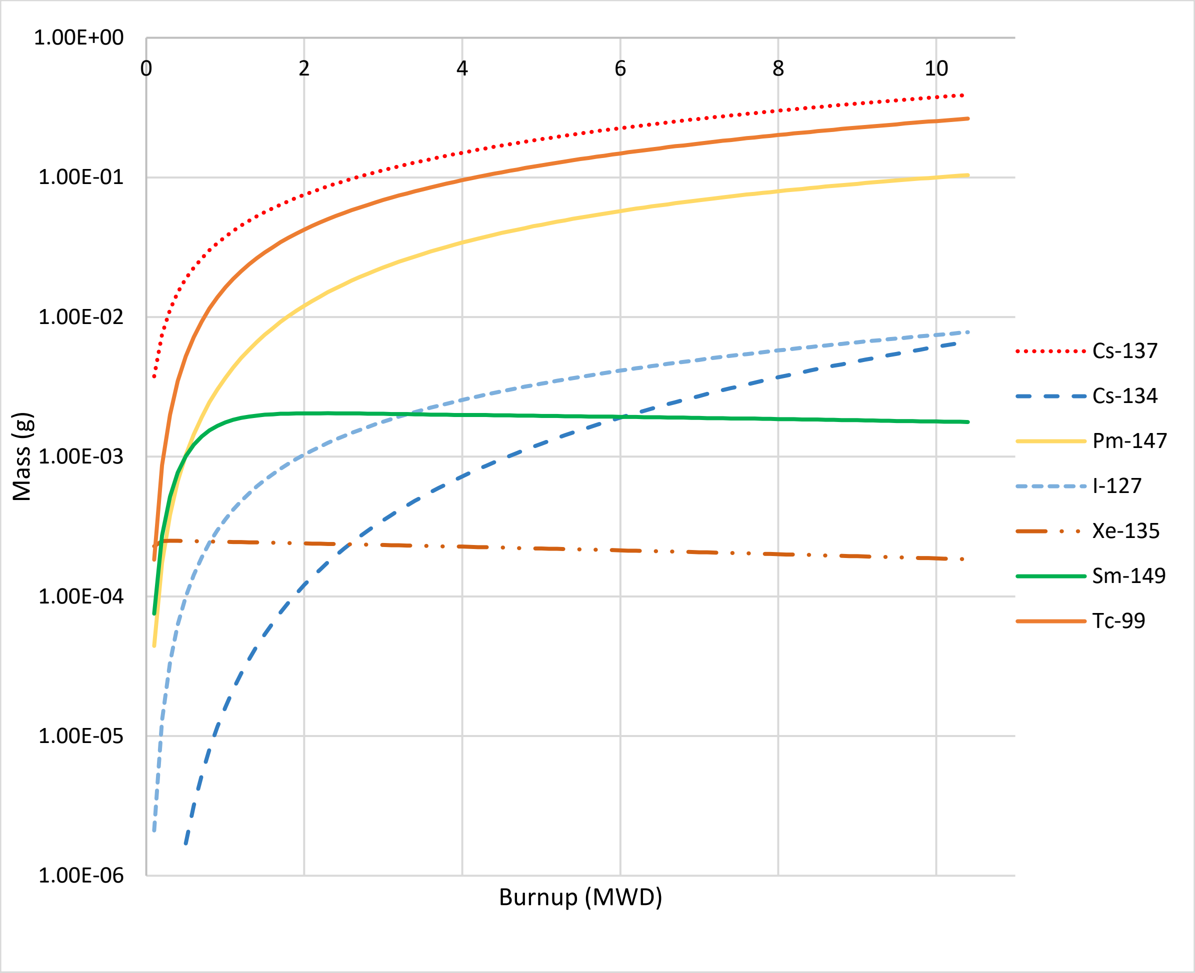

Figure 11: Major fission products inventory in fuel number #109

Table 1: Total RTP fuel's gamma energy and strength after 1-year decay

Gamma energy (KeV)	Gamma/second	Fraction
21.54	1.61E+08	1.21E-06
29.97	5.62E+05	4.23E-09
40.98	1.49E+11	1.12E-03
45.3	1.75E+09	1.32E-05
57.63	2.19E+10	1.65E-04
64.28	1.22E+06	9.17E-09
80.12	7.81E+11	5.87E-03
86.55	4.10E+10	3.08E-04
86.94	1.13E+06	8.50E-09
87.57	4.71E+06	3.54E-08
105.31	2.82E+10	2.12E-04
105.5	1.18E+08	8.87E-07
123.07	7.44E+08	5.59E-06
133.51	6.36E+12	4.78E-02
145.44	1.91E+11	1.44E-03
162.66	2.48E+05	1.86E-09
204.1161	4.07E+07	3.06E-07
235.69	3.51E+10	2.64E-04
427.87	1.25E+12	9.40E-03
484.471	4.05E+07	3.05E-07
497.08	6.44E+12	4.84E-02
537.26	9.72E+05	7.31E-09
550.27	6.75E+10	5.08E-04
556.65	1.01E+08	7.59E-07
557.06	5.94E+10	4.47E-04
561.9	2.18E+07	1.64E-07
569.33	1.66E+12	1.25E-02
600.6	7.48E+11	5.62E-03
604.72	1.05E+13	7.89E-02
610.33	4.08E+11	3.07E-03
629.97	6.33E+10	4.76E-04
635.95	4.75E+11	3.57E-03
661.66	8.13E+13	6.11E-01
695.88	2.61E+09	1.96E-05
723.3	3.69E+08	2.77E-06
724.19	5.76E+12	4.33E-02
725.7	2.34E+10	1.76E-04
729.57	5.89E+08	4.43E-06
756.73	7.07E+12	5.32E-02
765.803	1.45E+11	1.09E-03
795.86	9.23E+12	6.94E-02
908.96	3.68E+08	2.77E-06
933.838	2.79E+08	2.10E-06
1088.64	6.90E+07	5.19E-07
1204.77	2.06E+10	1.55E-04
1274.43	6.41E+08	4.82E-06
Total intensity	1.33E+14	1.00E+00

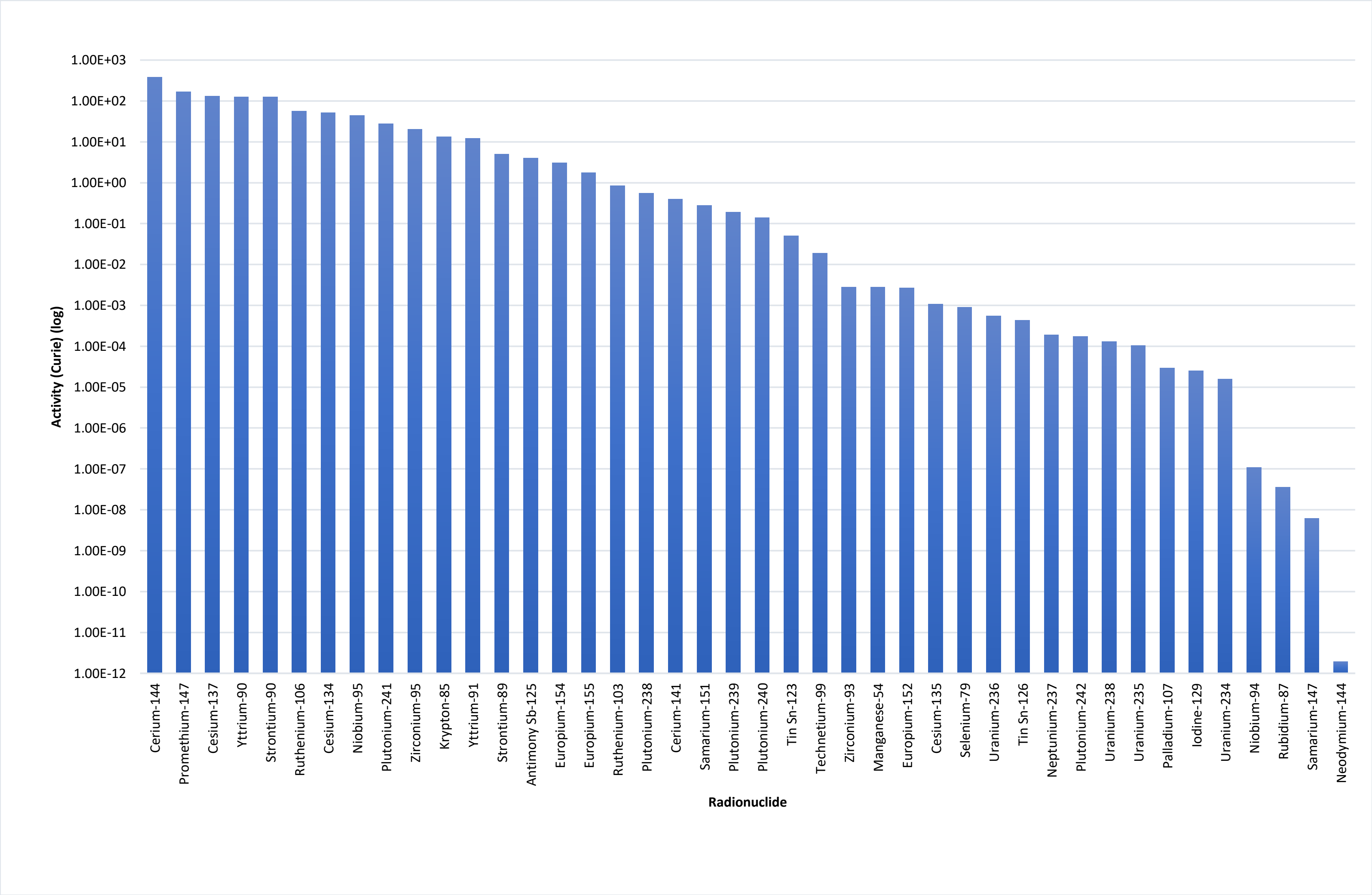

Figure 12: Fission product inventory for a single 20 wt% fuel rod at 50% burnup after 1-year cooling period.

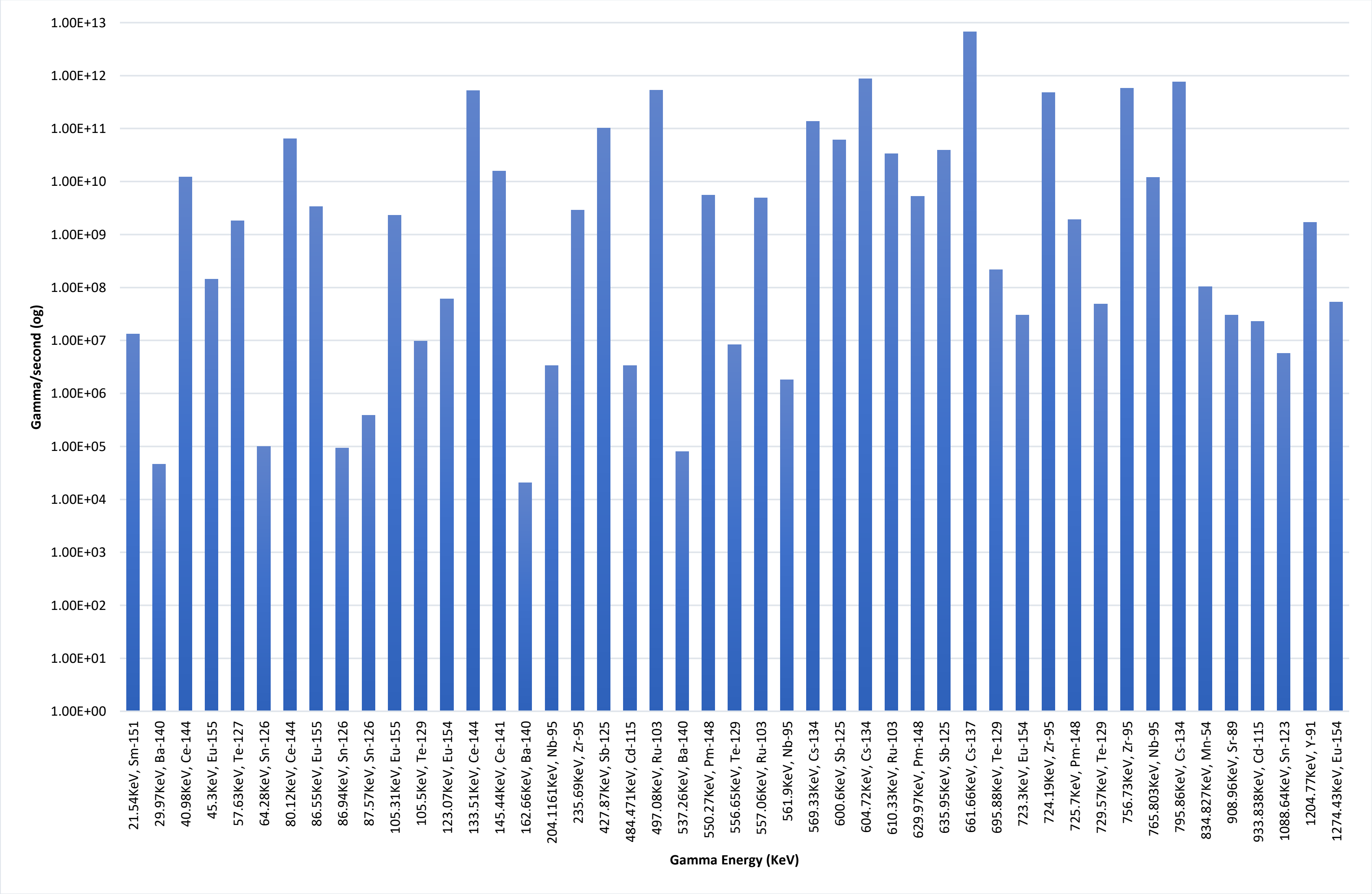

Figure 13: Gamma energy distribution and major intensities for a single 20 wt% fuel rod at 50% burnup after a 1-year cooling period.

Determination of decay heat in SFP

Gamma radiation propagates from the source at the bottom of the SFP, traveling in all directions through the water medium, before being absorbed by the stainless-steel lining. As the gamma radiation travels, part of its energy is absorbed by the surrounding materials, resulting in energy deposition. Since gamma radiation is more effectively absorbed by high-density materials, areas with higher density exhibit greater energy deposition, leading to higher decay heat (Ihsani et al., 2024). This phenomenon is illustrated in Figure 14, where decay heat decreases progressively with increasing distance from the source. However, the stainless-steel lining, being of higher density than water, may exhibit slightly higher decay heat compared to closer segments (e.g., volumes E, F, and G) due to its superior energy absorption properties. The density of stainless steel allows for more efficient gamma energy absorption and deposition, contributing to this localized increase in decay heat. Additionally, the gamma source is supported by the fuel rack, which is constructed from stainless steel within the SFP. As a result, the fuel rack is expected to experience the highest decay heat compared to all other volume segments. However, the analysis of the rack's thermal response and mass load will be addressed in future work.

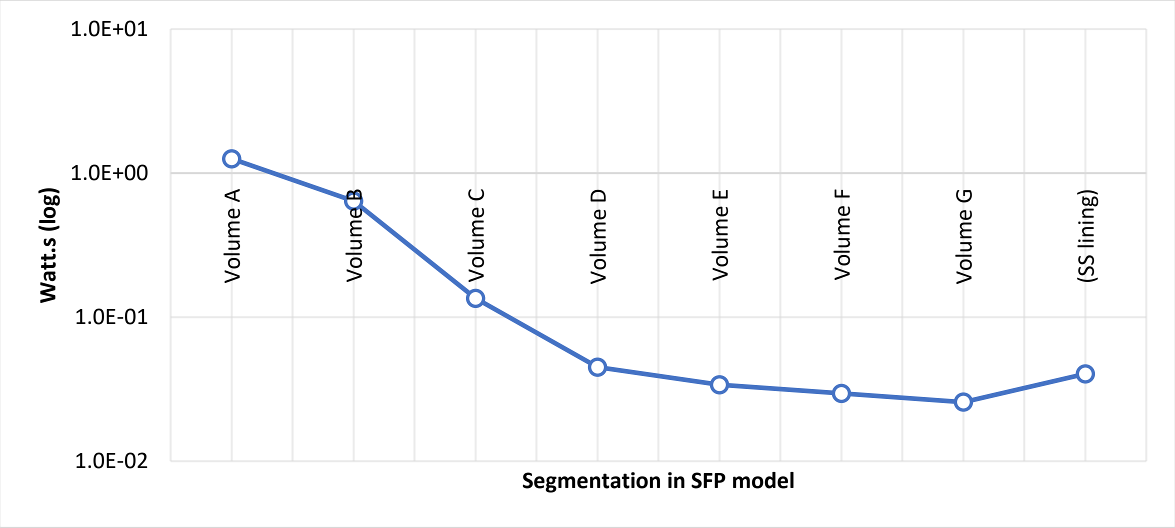

Figure 14: Total decay heat generated in each volume segment of the SFP model.

Determination of decay heat in FTC (lead) and in concrete

Figure 15 illustrates the decay heat trends for three different materials: lead (~11 g/cc), normal concrete (2.3 g/cc), and high-density concrete (3.4 g/cc). The maximum decay heat occurs in the innermost layer of the lead shield in the FTC, where it exponentially decreases with increasing distance from the source. In contrast, concrete materials, having lower density, allow more gamma radiation to pass through and deposit energy at greater distances from the inner layer. As a result, within the first 2 cm of thickness, concrete exhibits lower decay heat compared to lead (Bakos, 2006). However, as the distance increases, the decay heat in concrete does not decrease as rapidly as it does in lead, due to the lower energy absorption efficiency of concrete.

This phenomenon also applies to variations in density within the same material, such as concrete. In this case, high-density concrete exhibits higher decay heat than normal concrete within the first 8 cm. Beyond 9 cm, the decay heat in normal concrete surpasses that of high-density concrete, and the two curves diverge further as the distance increases.

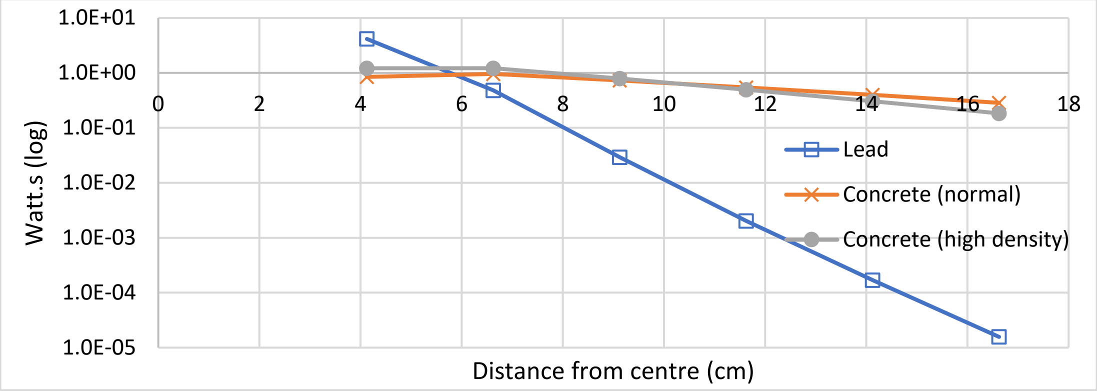

Figure 15: Decay heat variation as a function of distance for different materials in the single fuel case.

CONCLUSIONS

In conclusion, this study evaluates the radiation decay heat from TRIGA reactor fuel to aid in future handling procedures. It successfully determines the radiation source term for the current RTP fuel inventory and individual fuel elements under extreme burnup conditions. Additionally, the study assesses the energy deposition from decay heat within both the SFP and FTC. The simulation process for estimating decay heat in the SFP starts with reactor operation history data, which informs TRIGLAV calculations and determines the core burnup and individual fuel element burnup. Using the calculated burnup, the radionuclide inventory is assessed with the MCNPX CINDER90 code, and gamma radiation intensity and energy spectra are evaluated to estimate decay heat.

The detailed radionuclide inventory generated by MCNPX provides a comprehensive understanding of the isotopes present in irradiated TRIGA fuel elements, including their buildup and decay over time. Actinides such as U-236 and Pu-239 are identified as significant contributors to the fuel's composition, with the majority of gamma radiation arising from the decay of fission products like iodine-131 and cesium-137. The gamma energy spectrum, compiled from established databases, reveals that after one year of decay, the 661.66 keV gamma radiation is the most prominent, accounting for a substantial portion of the total emitted gamma radiation.

The gamma radiation is absorbed more effectively by higher-density materials, such as the stainless-steel lining, leading to increased decay heat compared to surrounding segments. Lead exhibits the highest decay heat near the source, with heat decreasing exponentially as distance increases, while concrete allows more gamma radiation to penetrate, resulting in lower decay heat initially but a slower decrease over distance.

A detailed analysis and simulation are currently underway to further investigate the properties of the source term, including the effects of axial burnup distribution. Additionally in the future, the study aims to explore various structural configurations and materials within the defined scope.

ACKNOWLEDGEMENTS

The author would like to express gratitude to the Reactor Technology Centre of the Malaysian Nuclear Agency for their support of this study.

REFERENCES

Bakos, G. C. (2006). Calculation of γ radiation converted to thermal energy in nuclear reactor shielding facilities. *Annals of Nuclear Energy*, *33*(3), 236–241.

El Maliki El Hlaibi, S., Lamkaddam, O., El Bardouni, T., Chakri, A., & Misdaq, M. A. (2023). Calculation of the activity inventory of the CENM TRIGA MARK II reactor for decommissioning planninig. *Radiation Physics and Chemistry*, *207*, 110837.

IAEA. (2014). *Project Experiences in Research Reactor Ageing Management, Modernization and Refurbishment*.

IAEA. (2016). *History, Development and Future of TRIGA Research Reactors* (No. 482). Vienna, Austria: IAEA

IAEA. (n.d.). TRIGA REACTOR CHARACTERISTICS. Retrieved from https://ansn.iaea.org/Common/documents/Training/TRIGA Reactors (Safety and Technology)/pdf/chapter1.pdf

Ihsani, R. N., Gareso, P. L., & Tahir, D. (2024). An overview of gamma radiation shielding: Enhancements through polymer-lead (Pb) composite materials. *Radiation Physics and Chemistry*, *218*, 111619.

Pelowitz, D. B. (2011). *MCNPX TM User's manual version 2.7.0*. Los Alamos, NM, USA: Los Alamos Scientific Laboratory.

Pungerčič, A., Čalič, D., & Snoj, L. (2020). Computational burnup analysis of the TRIGA Mark II research reactor fuel. *Progress in Nuclear Energy*, *130*, 103536.

Rabir, M. H., Muttaqin, A., Bayar, J., & Karim, J. A. (2022). In-Core Rtp Fuel Relocation and Criticality Behaviour Using Mcnp5 / X Code. *Jurnal Nuklear dan Teknologi Relatif*, *19*(1), 8–18.

Rochman, D., Hursin, M., Pillon, S., St-Jean, C., Leconte, P., & Serot, O. (2024). An introduction to Spent Nuclear Fuel decay heat for Light Water Reactors: a review from the NEA WPNCS. *EPJ Nuclear Sciences & Technologies*, *10*, 9.

Jurnal Sains Nuklear Malaysia, 2025, 37(No.1): 50 – 60
ISSN: 2232-0946

ANALYSIS OF CYCLE LENGTH FOR HIGH-FISSILE-DENSITY FUEL IN HTR-MMR

Mohamad Hairie Rabir*, Mark Dennis Usang and Julia Abdul Karim

Reactor Technology Centre, Malaysian Nuclear Agency,
Bangi, 43000 Kajang, Selangor, Malaysia
*Correspondence author: m_hairie@nm.gov.my

ABSTRACT

Micro Modular Reactors (MMRs) are gaining significant attention in the nuclear power industry due to their compact design and mobility. However, the challenge of optimizing neutron economy in such reactors remains a critical issue. To address this, advanced fuel designs with higher fissile density are being explored to extend the operational cycle length of MMRs. This paper presents a detailed neutronics simulation of an MMR using High-Fissile-Density Fuel. A High Temperature Reactor (HTR)-based MMR was selected as the reference model. Several case studies involving different High-Fissile-Density Fuel types were conducted, analyzing key neutronic parameters such as cycle length, achievable burnup, power distribution, and nuclide inventory. The simulations also examined the fuel temperature reactivity coefficient to assess the safety and efficiency of the proposed fuels. Thermal power generation and thermal-hydraulic behavior were not considered in this study and are left for future work. Results indicate a significant improvement in cycle length and burnup with the implementation of High-Fissile-Density Fuel, along with a more favorable power distribution. These findings suggest that advanced fuel designs could play a crucial role in enhancing the performance and sustainability of MMRs, contributing to the advancement of small nuclear reactor technologies.

Keywords: Neutronics, MCNPX, High density fuel, MMR reactor

INTRODUCTION

Micro Modular Reactors

Nuclear power is a key component of the low-carbon energy solution, having grown significantly in the 1970s and 1980s. Countries like China and South Korea have effectively expanded their nuclear capacity, with China doubling its capacity to 54 GWe by 2020. Innovations in nuclear technology focus on faster construction through factory production, simpler operation, and inherently safer designs. Small Modular Reactors (SMRs), which produce up to 300 MWe, are developed for their cost-effectiveness, safety, and versatility. Micro-sized Modular Reactors (MMRs), producing less than 30 MWe, offer advanced features like unmanned operations and emergency power supply. These advancements aim to enhance nuclear power's efficiency, safety, and economic viability (Rabir, Ismail & Yahya, 2021).

The High-Temperature Reactor (HTR) is the most studied MMR type due to its potential and suitability. It is considered a leading innovative reactor design, capable of deployment within a decade. Studies over the past 30 years have confirmed the inherent safety features of micro modular HTRs. They can co-generate industrial heat along with electricity. Despite being a mature design, further research is needed to improve its fuel burnup performance, as smaller reactors suffer from larger neutron leakage, affecting their burnup performance and operational cycle length. To extend the operational cycle, small reactors often operate at reduced power density, which decreases their fuel economics compared to commercial reactors (Rabir, Ismail & Yahya, 2021).

Advanced fuel to prolong cycle length

Utilizing high enriched uranium (HEU) fuel poses significant proliferation risks. Since the 1970s, numerous HEU fuels have been converted to low enriched uranium (LEU). Any enrichment level exceeding 20% uranium-235 is classified as HEU (Van Den Berghe & Lemoine, 2014). While most commercial large reactors currently use fuel with less than 5% U-235, new High Assay Low Enriched Uranium (HALEU) fuels are being developed to enhance reactor performance. The higher concentration of fissile U-235 in HALEU allows for smaller fuel assemblies and reactors, reducing the frequency of refueling. This makes HALEU an attractive option for many SMRs and MMRs. When paired with high-fissile-density fuels like uranium silicide (U_3Si_2) or uranium mononitride (UN), HALEU maximizes fuel performance due to their higher uranium densities—11.3 g/cm³ for U_3Si_2 and 13.55 g/cm³ for UN, compared to UO_2's 9.75 g/cm³.

Both UN and U_3Si_2 are promising candidates for advanced systems, including liquid-metal-cooled fast reactors. For UN, high linear heat generation rates—42 kW/m in lead-cooled and 54 kW/m in sodium-cooled reactors—are achievable due to its exceptional thermal properties. U_3Si_2 also supports high heat generation rates and demonstrates excellent mechanical integrity under high temperatures and irradiation conditions. The superior thermal conductivity of both materials ensures lower fuel temperatures, reduced thermal stresses, and enhanced safety margins, making them strong contenders for improving the efficiency and safety of light water and advanced reactor designs (Yang et al., 2021; Khoshahval, 2024) .

This research aims to simulate and compare the neutronics performance of three HTR-MMR core models loaded with different fuel types: UO_2, U_3Si_2, and UN. The study will analyze key parameters, including reactivity, neutron flux spectrum, and burnup, to determine the advantages of each fuel type.

METHODS

Select High Temperature Reactor (HTR) MMR as references reactor

The reference reactor core parameters are based on a micro-sized HTR prismatic block reactor, commonly known as the U-Battery, initially developed in 2008 and recognized for its commercialization potential among micro-HTR designs. This reactor technology uses graphite blocks as the moderator, with fuel blocks featuring channels for helium coolant and fuel compacts containing TRISO (TRi-structural ISOtropic) fuel particles embedded within a graphite matrix. TRISO (TRi-structural ISOtropic) fuel particles are advanced nuclear fuel designed for high-temperature reactors (HTRs). Each particle consists of a fissile kernel surrounded by three protective layers: an inner porous carbon buffer, pyrolytic carbon layers (PyC), and a silicon carbide (SiC) layer. These layers ensure excellent fission product retention, with containment efficiencies exceeding 99.9%, and enable operation at temperatures up to

1600°C. The particle size is typically ~0.92 mm, and their design enhances safety and fuel integrity under extreme conditions (Kabach et al. 2021).

The fuel quantity depends on the concentration of TRISO particles, characterized by the "packing fraction" parameter. The TRISO packing fraction refers to the volume fraction of TRISO fuel particles within a fuel compact or matrix, typically ranging from 30% to 40% in high-temperature reactor designs to balance fuel performance, heat transfer, and structural integrity. The annular core configuration consists of six fuel columns surrounded by reflector blocks, with an additional central reflector block, as illustrated in Figure 1 (Ding & Kloosterman, 2011). For this study, each column comprises two stacked fuel blocks, resulting in a total of 12 fuel blocks, reduced from the original larger configuration to minimize simulation time since core design optimization is not the study's focus. The U-Battery's fuel blocks are modeled after the gas turbine-modular helium reactor (GT-MHR) design, with detailed parameters provided in Tables 1 and 2 (Ding & Kloosterman, 2013).

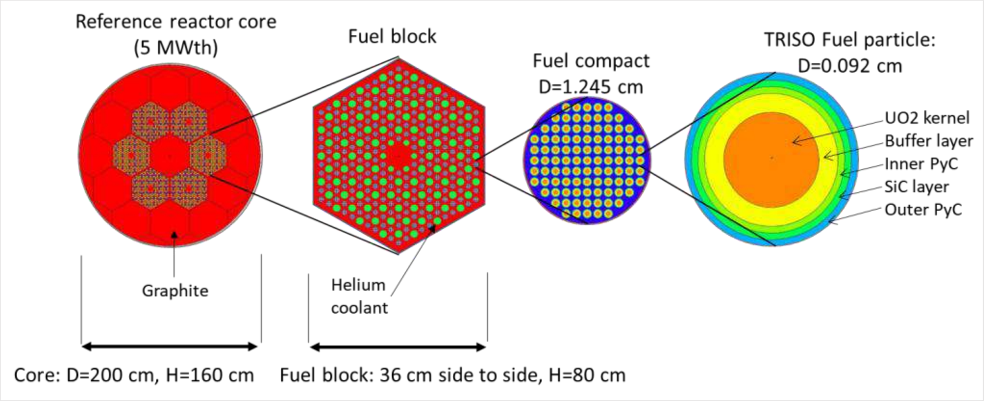

Figure 1 Reference reactor core configuration of the U-Battery

Table 1 MMR reference reactor core parameters

Parameter	Details
Reactor type	Block-type HTR
Thermal power	5 - 10 MWth
Cycle length	5 – 10 years
Core configuration	Annular core, 6 columns
Fuel type	UO_2, TRISO particle
Fuel enrichment	< 20 wt% $^{235}U/U$
Coolant	Helium
Inlet/outlet temperature	250/750 ˚C
Energy utilization	Electricity, process heat

Table 2 Fuel block parameters

Parameter	
Width across flats (cm)	36
Height of block (cm)	80
Fuel kernel radius (µm)	250
Buffer layer thickness (µm)	100
Buffer layer density (g/cm3)	1
Inner PyC layer thickness (µm)	35
Inner PyC layer density (g/cm3)	1.9
SiC layer thickness (µm)	35
SiC layer density (g/cm3)	3.2
Outer PyC layer thickness (µm)	40
Outer PyC layer density (g/cm3)	1.97
Fuel compact diameter (cm)	1.245
Fuel compact height (cm)	4.93
TRISO packing fraction (%)	30

Simulation tool and model

All calculations were conducted using the MCNPX 2.7 code with the ENDF/B-VII.0 nuclear data library for steady-state reaction simulations. Key parameters such as neutron flux, reaction rates, and eigenvalues were calculated, while isotope depletion and updated isotopic compositions of the fuel were determined using the CINDER90 burnup code integrated with MCNPX. Due to the core's geometric symmetry, only 1/6 of the core was simulated, representing a single column of two stacked fuel blocks. This column was divided into segments, with each segment serving as a burnup zone where material changes occur independently, corresponding to spatial flux variations during the burnup period. Reflective boundary conditions were applied, with no burnable absorbers and a standardized fuel block temperature of 600°C. The MCNPX model simulated a high-temperature reactor core with detailed geometry, including the compact fuel's explicit TRISO arrangement. Burnup calculations using MCNPX KCODE achieved standard deviations ranging from 0.00040 to 0.00050 (40–50 pcm) with 50000 neutrons per cycle, 150 cycles, and 50 skipped cycles.

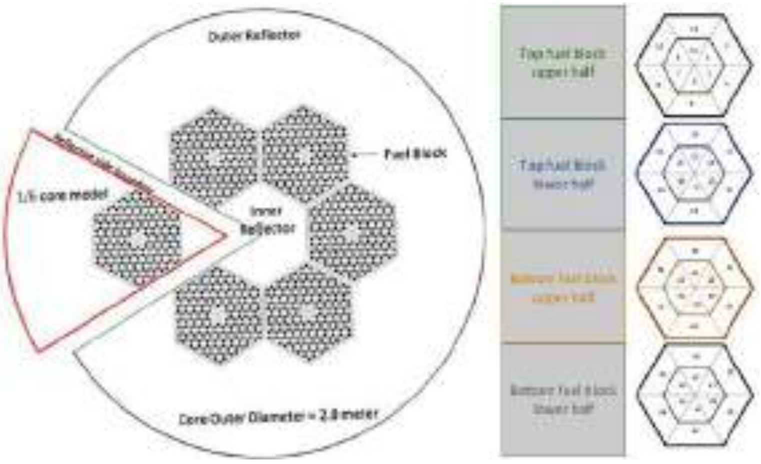

Figure 2: Top view of the referenced core illustrating the 1/6 model used in the MCNPX simulation (left) and the burnup zoning scheme applied (right), divided into four axial segments and six radial segments, numbered from 1 to 48.

Neutronics parameters

In this work, we analyzed several key neutronics parameters to highlight the differences between the fuel materials evaluated. The effective multiplication factor (k_{eff}) measures how the neutron population changes from one generation to the next in a nuclear reactor. The k_{eff} determines how long a reactor can sustain a chain reaction, directly influencing cycle length. Cycle length and exit burnup, measured in effective full power years (EFPY) and gigawatt-days per ton of heavy metal (GWd/tHM), are critical for determining the operational lifespan of the reactor core and the energy extracted per unit of fuel. EFPY is a unit of time that represents how long a nuclear reactor or fuel has operated at 100% full power continuously. It accounts for actual operating conditions by normalizing part-power or intermittent operation to an equivalent period at full power. The neutron flux energy spectrum expressed in neutrons flux unit with energy in MeV, describes how neutrons are distributed across various energy levels within the reactor. Fissile inventory, quantified in kilograms or grams, indicates the total mass of fissile material in the core, which is essential for assessing reactivity and fuel consumption. The peaking factor represents the peak local power within the reactor core, reflecting the maximum power density at specific locations compared to the average power across the core. Finally, the fuel temperature coefficient (FTC), expressed in pcm/°C, represents how reactivity changes with temperature variations in the reactor core. This analysis is limited to neutronics, as the study is in a preliminary stage; aspects related to heat management and thermal-hydraulic behavior are not included and are left for future investigation.

RESULTS AND DISCUSSION

Cycle length and burnup

Figure 3 illustrates the variation of k_{eff} over time for UO_2, U_3Si_2, and UN-loaded cores. As power is generated from fission, the buildup of xenon leads to a rapid decrease in k_{eff}. Subsequently, fuel depletion occurs, resulting in a slower, more gradual decline in k_{eff}. Among the fuel types, UO_2 exhibits the highest k_{eff} at the beginning of cycle (BOC), despite having a lower fissile mass than the other configurations. This behavior can be attributed to the reduced resonance capture associated with the lower U-238 mass in UO_2, which allows for a greater availability of thermal neutrons to induce fission.

In contrast, fuels with higher fissile densities, such as U_3Si_2 and UN, experience increased competition between resonance capture and neutron thermalization. This competition results in a lower k_{eff} at BOC as fissile density increases, despite the higher U-235 content. Nevertheless, the k_{eff} trends for U_3Si_2 and UN cores exhibit a gentler slope, indicating slower depletion compared to the UO_2 core. This slower depletion rate contributes to an extended cycle length, as evidenced by the UN-loaded core achieving the longest EFPY of 3.45. Meanwhile, the U_3Si_2-loaded core begins with the lowest k_{eff} at BOC. Although its depletion rate is less pronounced, it achieves a similar cycle length to the UO_2-loaded core, approximately 2.75 EFPY.

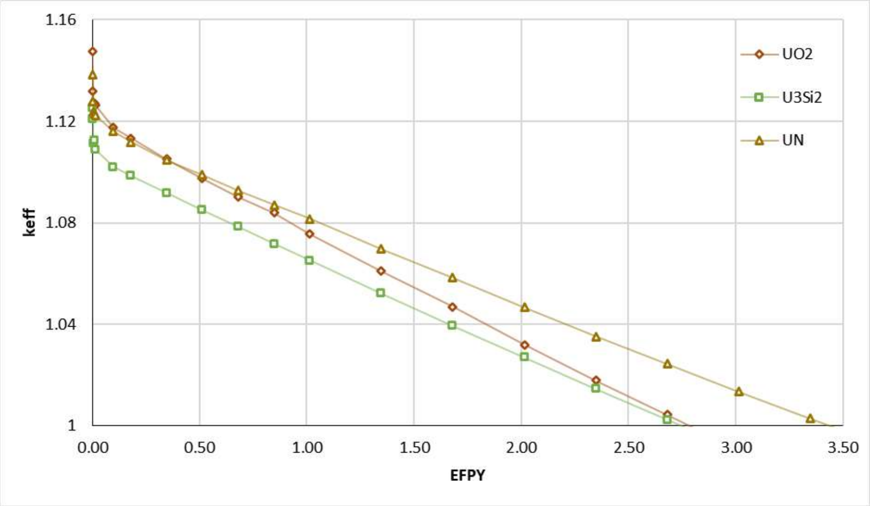

Figure 3: Evolution of k_{eff} over time for UO_2, U_3Si_2, and UN-loaded cores

Figure 4 depicts the average core burnup over time, measured in effective full-power years (EFPY), for the three cases. Since all cores operate at the same thermal power (simulated at 5 MWth), cores with higher fuel density exhibit a lower burnup gradient due to their larger initial fuel mass. Notably, the UN-loaded core achieves an exit burnup of approximately 60 GWd/MTU, which is remarkably high and within the range of advanced fuel burnup performance. In comparison, the UO_2-loaded core achieves an exit burnup of around 47 GWd/MTU, similar to the U_3Si_2-loaded core. Despite its lower burnup gradient compared to UO_2, the U_3Si_2-loaded core demonstrates a steeper gradient than the UN-loaded core.

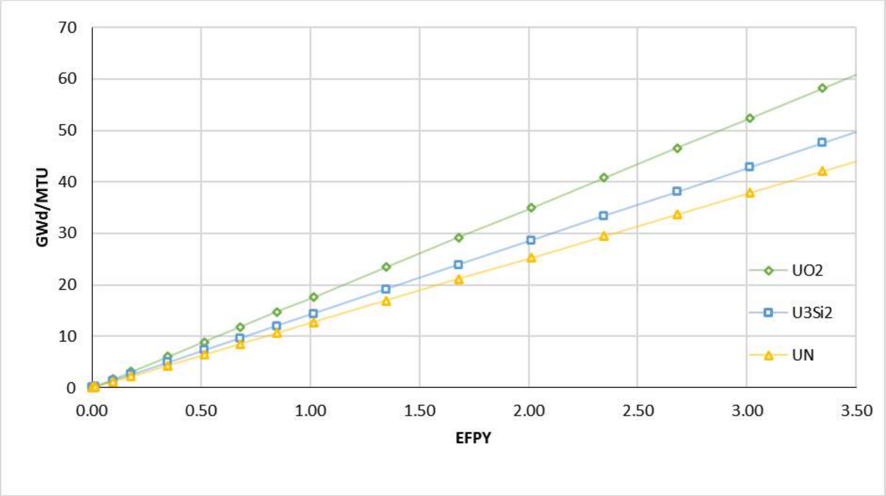

Figure 4: Average core burnup as a function of time (EFPY)

Neutron spectrum

The spectrum profile aligns closely with the typical neutron spectra reported in the literature for HTR prismatic fuel blocks. Unlike water-moderated reactors, the transition from fast to thermal energy occurs relatively more rapidly, whereas HTRs with graphite moderation require longer scattering times. Consequently, a significant fraction of neutrons remains within the resonance energy region in the spectrum (Chiang et al., 2014; Kim, Cho & Venneri 2007). Higher fissile density fuels with greater U-238 mass, corresponding to increase resonance capture, result in fewer neutrons reaching thermal energy levels. This trend is illustrated in

Figure 5, where higher fissile density correlates with a reduction in neutron flux at energies below approximately 1E-4 MeV. To demonstrate the effect of increased fissile density, Figure 5(b) illustrates that, while UO_2 exhibits a higher peak in the thermal neutron group at the EOC compared to the BOC, indicating an increase in thermal neutron flux, the other two materials show slightly lower peaks at EOC relative to BOC. In UO_2, the primary contribution to neutron absorption is from U-235. As U-235 depletes, the thermal neutron absorption reaction is significantly reduced. This trend is also expected to occur in U_3Si_2 and UN; however, in these materials, the contribution of resonance capture remains significant compared to the absorption in U-235.

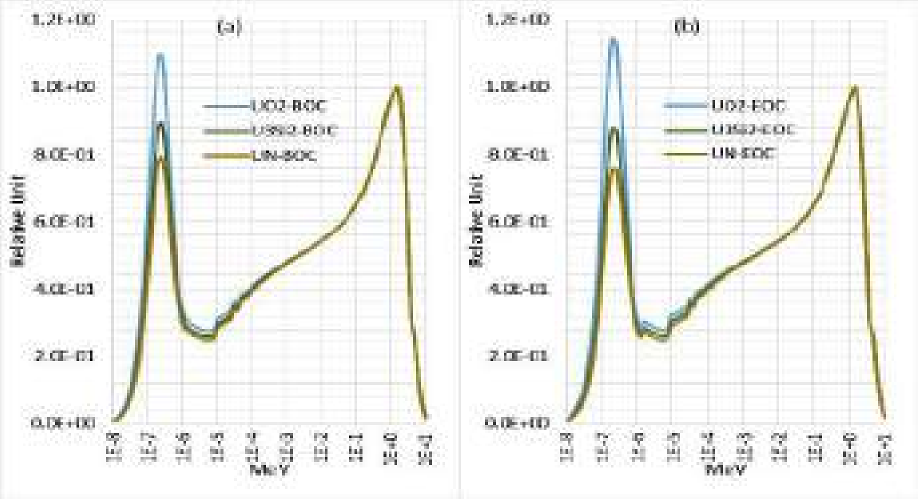

Figure 5: Neutron energy spectrum at beginning of cycle (BOC) and end of cycle (EOC).

Power distribution

Figure 6 illustrates the trends in the highest radial power peaking factor and its variation over time, expressed in effective full power years (EFPY). The results do not represent the actual spatial power distribution or its variation as a function of area or volume. Instead, they provide a single data point reflecting the highest power peak relative to the average and its evolution over time, as well as with burnup and depletion. It should be noted that none of the core models are optimized and all share the same basic configuration and fuel block loading pattern. As a result, the power distribution is expected to show minimal variation. However, fuels with higher fissile density exhibit slightly elevated maximum radial power peaking trends across the entire cycle length, which can lead to higher local fuel temperatures due to increased heat generation in those regions.

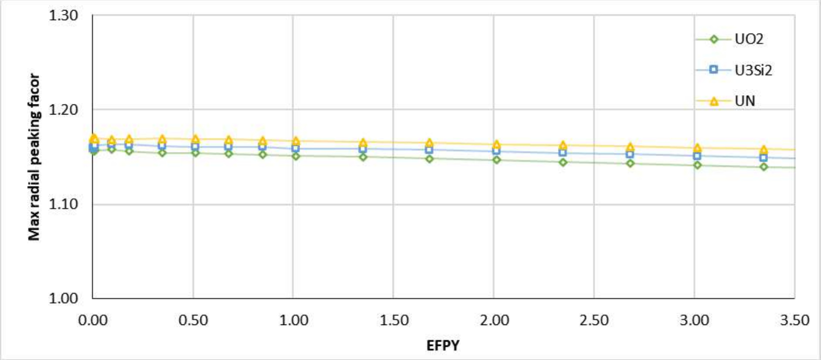

Figure 6: Comparison of the highest power peaking factor and its variation over time (EFPY).

Major fissile inventory

The concentrations of major fissile actinides as a function of cycle length are presented in Figure 7. The exponential depletion trends of U-235 for all core models are shown in Figure 7(a). It can be observed that fuels with relatively lower initial U-235 mass exhibit a progressively steeper depletion trend. As expected, Figures 7(b) and 7(c) indicate that Pu-239 build-up is highest in U_3Si_2 and UN loaded cores due to their higher U-238 content. With an increased production of fissile isotope Pu-239, the depletion of U-235 is relatively slower in these fuels, as the plutonium contributes significantly to the total fission process (Uguru et al., 2020).

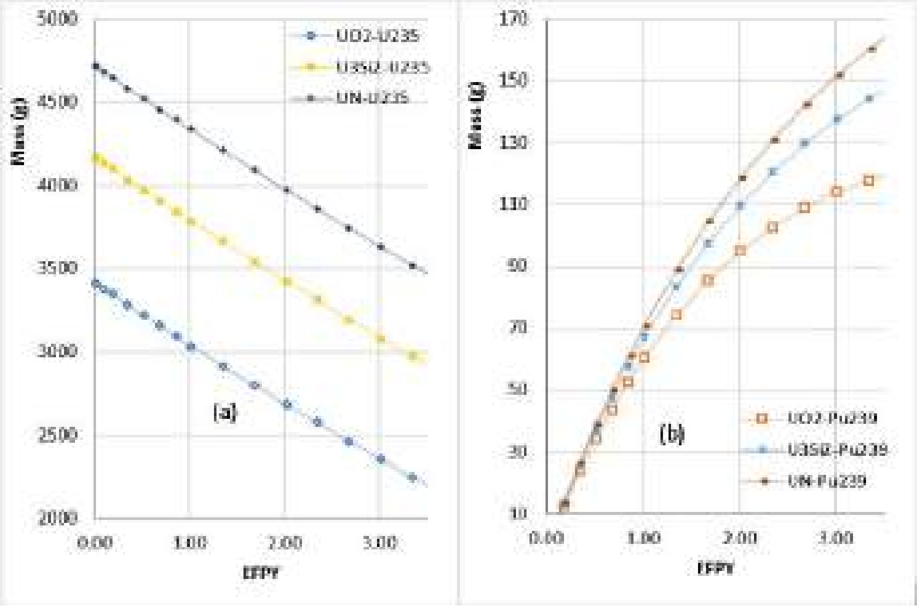

Figure 7: Reactors major fissile inventory comparison

Fuel temperature reactivity coefficient

The FTC calculated in this work are derived from differences in k_{eff} results obtained through simulations conducted at two temperatures: 600°C and 900°C. In this section of the calculation, the k_{eff} results obtained from MCNPX simulations were converted to reactivity (ρ) expressed in pcm (1E5 $\Delta k/k$). Figure 8 illustrates the simulated FTC values plotted against cycle length for three core models, all of which exhibit consistently negative FTCs throughout irradiation. As burnup progresses, the Doppler effect becomes more pronounced (FTC values become increasingly negative) due to contributions from U-238 and the accumulation of other non-fissile actinides (Choi, 2011). The FTC values obtained in this study align well with results reported for reference reactors in previous studies (Ding et al. 2011; Rabir, Ismail & Yahya, 2021). In comparison to UO_2, cores loaded with U_3Si_2 and UN demonstrate relatively stronger Doppler effects. This is evident from the more negative FTC values scattered throughout the cycle length for these fuels. The enhanced Doppler effect is attributed to the higher U-238 mass in U_3Si_2 and UN fuels, leading to increased resonance capture as the temperature rises.

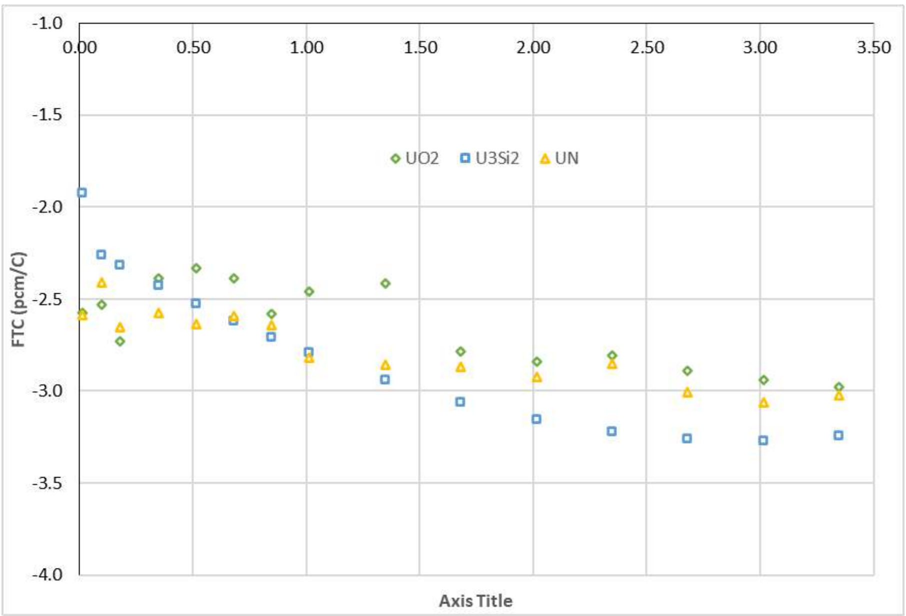

Figure 8: FTC trends comparison

Application-Oriented Fuel Selection

Based on the findings, UN (Uranium Nitride) emerges as the most suitable fuel candidate for nuclear power applications, particularly in Micro Modular Reactors (MMRs), due to its superior cycle length, high burnup capability, and strong negative fuel temperature coefficient, which enhances safety. Its high fissile density and thermal conductivity make it ideal for power reactors where long operating cycles and thermal performance are critical. Conversely, U_3Si_2 (Uranium Silicide), with its favorable neutronic behavior and moderate burnup, may be more appropriate for research reactors, where shorter cycles, higher neutron flux, and flexibility in reactivity management are often prioritized.

CONCLUSIONS

MMRs are gaining prominence in nuclear power applications due to their compact design and mobility. However, optimizing neutron economy remains a significant challenge. This study evaluates the performance of High-Fissile-Density Fuels (U_3Si_2 and UN) in HTR-based MMRs through detailed neutronics simulations. Key parameters assessed include reactivity, burnup, neutron flux spectrum, and safety metrics such as power distribution and the fuel FTC.

The results indicate that UN-loaded cores achieve the longest cycle length (3.45 EFPY) and highest exit burnup (60 GWd/MTU). While the U_3Si_2 core begins with a lower k_{eff} at the BOC compared to UO_2, it achieves a similar cycle length (2.75 EFPY) due to its slower depletion rate. Neutron spectrum analysis reveals that fuels with higher fissile density and greater U-238 content exhibit increased resonance capture, resulting in reduced thermal neutron flux. This is particularly evident in U_3Si_2 and UN fuels, which display lower thermal peaks at EOC compared to BOC. Higher-density fuels also exhibit slightly elevated maximum radial power peaking factors.

All core models demonstrate consistently negative FTCs throughout irradiation, with more pronounced negative values for U_3Si_2 and UN cores, attributed to their higher U-238 content. This indicates stronger Doppler effects, enhancing reactor stability at elevated temperatures. While High-Fissile-Density Fuels show potential for improving cycle length, burnup, and safety characteristics, further research is required to optimize material composition and core design before these findings can be generalized.

ACKNOWLEDGEMENTS

The author would like to express gratitude to the Reactor Technology Centre of the Malaysian Nuclear Agency for their support of this study.

REFERENCES

Bomboni, E., Cerullo, N., Lomonaco, G., & Romanello, V. (2008). A Critical Review of the Recent Improvements in Minimizing Nuclear Waste by Innovative Gas-Cooled Reactors. *Science and Technology of Nuclear Installations*, *2008*, 1–18.

Chiang, M. H., Wang, J. Y., Sheu, R. J., & Liu, Y. W. H. (2014). Evaluation of the HTTR criticality and burnup calculations with continuous-energy and multigroup cross sections. *Nuclear Engineering and Design*, *271*, 327–331.

Choi, H. (2011). Advanced fuel cycle scenarios for High Temperature Gas Reactors. *Annals of Nuclear Energy*, *38*(11), 2338–2349.

Ding, M., & Kloosterman, J. L. (2011). Neutronic feasibility design of a small long-life HTR. Nuclear Engineering and Design, 241(12), 5093–5103.

Ding, M., & Kloosterman, J. L. (2013). Feasibility neutronic design for the reactor core configurations of a 5 MWth transportable block-type HTR. *Nuclear Science and Technology*, *24*(4), 1–6.

Ding, M., Kloosterman, J. L., Lathouwers, D., Lindley, E., & Perret, G. (2011). *Design of a U-Battery®*. Delft.

Kabach, O., Chetaine, A., Benchrif, A., Amsil, H., & El Banni, F. (2021). A comparative analysis of the neutronic performance of thorium mixed with uranium or plutonium in a high-temperature pebble-bed reactor. *International Journal of Energy Research*, *45*(11), 16824–16841.

Khoshahval, F. (2024). Neutron-physical characteristics of UO2 and UN/U3Si2 fuels with Zr, SiC and APMT accident tolerant claddings. *Radiation Physics and Chemistry*, *222*, 111869

Kim, Y., Cho, C., & Venneri, F. (2007). Long-Cycle and High-Burnup Fuel Assembly for the VHTR. *Journal of Nuclear Science and Technology*, *44*(3), 294–302.

Rabir, M. H., Ismail, A. F., & Yahya, M. S. (2021). Neutronics calculation of the conceptual TRISO duplex fuel rod design. *Nuclear Materials and Energy*, *27*, 101005.

Rabir, M. H., Ismail, A. F., & Yahya, M. S. (2021). A neutronic investigation of tristructural isotropic-duplex fuel in a high-temperature reactor prismatic seed-and-blanket fuel block configuration with reduced power peaking. *International Journal of Energy Research*, *45*(13), 19265–19288.

Rabir, M. H., Ismail, A. F., & Yahya, M. S. (2021). Review of the microheterogeneous thoria-urania fuel for micro-sized high temperature reactors. *International Journal of Energy Research*, *45*(8), 11440–11458.

Uguru, E. H., Sani, S. F. A., Khandaker, M. U., & Rabir, M. H. (2020). Investigation on the effect of 238U replacement with 232Th in small modular reactor (SMR) fuel matrix. *Progress in Nuclear Energy*, *118*, 103108.

Van Den Berghe, S., & Lemoine, P. (2014). Review of 15 Years of High-Density Low-Enriched UMo Dispersion Fuel Development for Research Reactors in Europe. *Nuclear Engineering and Technology*, *46*(2), 125–146.

Yang, K., Kim, Y., Park, H., Koo, Y., Kim, T., Jeong, S., & Sohn, D. (2021). Uranium nitride (UN) pellets with controllable microstructure and phase – fabrication by spark plasma sintering and their thermal-mechanical and oxidation properties. *Journal of Nuclear Materials*, *557*, 153272.

Jurnal Sains Nuklear Malaysia, 2025, 37(No.1): 61 – 68
ISSN: 2232-0946

RECOVERY OF NEODYMIUM AND DYSPROSIUM FROM ACETIC ACID LEACHING SOLUTION OF XENOTIME BY SOLVENT EXTRACTION

Khaironie Mohamed Takip[1*], Roshasnorlyza Hazan[1], Nur Aqilah Sapiee[1],
Jacqueline Kones[1], Norhazirah Azhar[1], Wilfred Paulus[1],
Nor Asniza Ariffin[2] and Muhammad Faiz Fadzel[3]

[1]Industrial Technology Division, Malaysian Nuclear Agency,
Bangi, 43000, Kajang, Selangor
[2]School of Chemical Engineering, Universiti Teknologi MARA,
Cawangan Sarawak, 94300 Kota Samarahan, Sarawak
[3]School of Chemical Engineering, Universiti Teknologi MARA,
Cawangan Terengganu, 23200 Bukit Besi, Dungun, Terengganu
*Correspondence author: khaironie@nm.gov.my

ABSTRACT

Rare earth elements (REEs) have become increasingly influential in human lives due to their significant roles in various high-tech applications. The research on neodymium (Nd) and dysprosium (Dy) recovery from either primary or secondary REE sources has attracted the increasing attention of researchers because of their importance and indispensable in the manufacturing of neo magnet or NdFeB. Solvent extraction after acid leaching is commonly applied to extract and separate Nd and Dy from different sources. Therefore, a study was conducted to recovery Nd and Dy from local xenotime minerals through solvent extraction. This research aimed to determine the ability of acetic acid (CH_3COOH) as the leaching solution for the recovery of Nd and Dy using an organic solvent, 30% of Di-(2-ethylhexyl) phosphoric acid (D2EHPA) in kerosene as the extractant. The Nd and Dy concentrations before and after extraction were analysed using Energy Dispersive X-Ray Fluorescence (EDXRF). The study found that the highest extraction efficiency of Nd and Dy was 99.4% and 99.3%, respectively, at the leaching solution concentration of 1M and the volume ratio of the aqueous-to-organic (A/O) phase equal to 1. The best extraction temperature and time with the optimum extraction efficiency was at 30°C and 20 min. Therefore, this study proves that CH_3COOH is potentially be used as the leaching media of xenotime for the extraction of Nd and Dy with D2EHPA.

Keywords: Neodymium; Dysprosium; Xenotime; CH_3COOH

Abstrak

Unsur nadir bumi (REE) telah menjadi semakin berpengaruh dalam kehidupan manusia oleh kerana peranan pentingnya dalam pelbagai aplikasi berteknologi tinggi. Penyelidikan mengenai perolehan semula neodimium (Nd) dan disprosium (Dy) daripada sumber REE utama atau sekunder telah menarik perhatian para penyelidik kerana kepentingan dan keperluannya dalam pembuatan magnet neo atau NdFeB. Pengekstrakan pelarut selepas larut lesap asid biasanya digunakan untuk mengekstrak dan memisahkan Nd dan Dy daripada sumber yang berbeza. Oleh itu, satu kajian telah dijalankan dengan mengekstrak Nd dan Dy daripada mineral xenotim tempatan melalui teknik pengekstrakan pelarut. Kajian ini bertujuan untuk menentukan keupayaan asid asetik (CH_3COOH) sebagai larutan larut lesap untuk *mengekstrak Nd dan Dy dengan pelarut organik, Di-(2-etilheksil) asid fosforik (D2EHPA) dalam kerosin dengan kepekatan 30%. Kepekatan Nd dan Dy sebelum dan selepas pengekstrakan dianalisis menggunakan Pendarfluor Sinar-X Penyebaran Tenaga (EDXRF). Kajian mendapati kecekapan pengekstrakan tertinggi Nd dan Dy ialah 99.4% dan 99.3%, pada kepekatan larutan larut lesap 1M dan nisbah isipadu fasa akueus-kepada-organik (A/O) bersamaan dengan 1. Suhu dan masa pengekstrakan terbaik dengan kecekapan pengekstrakan optimum ialah pada 30°C dan 20 min. Oleh itu, kajian ini membuktikan bahawa* CH_3COOH *berpotensi digunakan sebagai media larut lesap xenotim untuk mengekstrak Nd dan Dy dengan D2EHPA.*

Kata Kunci: Neodimium; Disprosium; Xenotim; CH_3COOH

INTRODUCTION

Rare earth elements (REE) are found in the Earth's crust at relatively low concentrations, with an estimated average concentration ranging from 150 to 220 parts per million (Qi, 2018). The most commonly mined REE-bearing minerals globally are bastnaesite, xenotime, and monazite, according to Balaram (2019). Due to their widespread use in the production of high-tech products such as computers, smartphones, permanent magnets, fluorescent lamp phosphors, electric vehicles, and renewable energy sources, REE have become a prominent area of focus in current research. Moreover, as they play a crucial role in the development of green technologies, more than 60% of REE demand is directed towards new applications and is expected to continue growing (Mancheri et al., 2019).

In Malaysia, xenotime is a commercially significant byproduct extracted from alluvial deposits, locally referred to as amang. This mineral is primarily found in the Kinta Valley of Perak State in Peninsular Malaysia.. Research by Hazan et al. (2019) has shown that local xenotime contains approximately 61.4% REEs with notable concentrations of yttrium (Y), ytterbium (Yb), dysprosium (Dy), erbium (Er), and neodymium (Nd) at 45.3%, 5.2%, 4.7%, 2.9%, and 1.6%, respectively. The growing demand for neodymium-iron-boron (NdFeB) permanent magnets, driven by the increasing use of electronic equipment and green energy technologies such as computers, wind turbines, and electric vehicles, has led to a surge in interest in extracting Nd and Dy from xenotime (Jowit et al., 2018). As a result, global production of NdFeB magnets is expected to experience rapid growth, driven by the rising demand for electronic devices and electric vehicles, according to Dushyantha et al. (2020). This trend is likely to have significant implications for the Malaysian mining industry, particularly in the extraction and processing of xenotime-rich amang deposits.

The extraction of Nd and Dy from xenotime typically involves a three-step process: digestion, separation, and extraction, as reported by Hazan et al. (2019). The initial step, digestion, aims to break down the orthophosphate mineral lattice into a byproduct called tri-sodium phosphate (Na_3PO_4). This process can be achieved through two methods: sulfuric acid baking or caustic digestion, as described by Farzaneh et al. (2017). However, a more recent approach has been using alkaline digestion with sodium hydroxide (NaOH) at high temperatures, also known as alkaline fusion digestion, which has been successfully applied to both xenotime and monazite processing (Hazan et al. 2019, Jacqueline et al. 2019, Azhar et al. 2020, Sanjit et al. 2021). This method is considered more effective for mineral decomposition, as it eliminates the need for evaporation and acid conversion, resulting in reduced liquid waste volumes, according to Mnculwane (2022).

Extraction of REE involves filtering a solution containing Na_3PO_4 to produce an insoluble REE hydroxide precipitate, followed by acidic leaching with non-organic acids such as sulfuric, hydrochloric, and nitric acids (Guan et al., 2022). Researchers have explored various methods for extracting REE from primary and secondary sources, including using organic acids like citric and acetic acid to leach waste materials (Gergoric et al., 2019; Stein et al., 2022). However, the application of organic acids for primary sources remains limited. For solvent extraction, reagents like D2EHPA, PC88A, and TOPO have been used extensively (Altansukh et al., 2021). D2EHPA is a popular choice due to its high extraction rate, selectivity, and stability (Pan-pan et al., 2018). This study investigated how factors such as acid concentration, aqueous-to-organic volume ratio, and temperature affect the extraction efficiency of neodymium (Nd) and dysprosium (Dy) using D2EHPA in kerosene as an extractant.

METHODOLOGY

Reagents And Instruments

This study used xenotime sand from Kinta Valley, Perak. Analytical-grade chemicals, including kerosene, NaOH, and CH_3COOH acid, were purchased from R&M Chemical while D2EHPA was obtained from Sigma Aldrich, Malaysia. The EDXRF (EDX-7000, Shimadzu) was used to analyze the sample's element concentrations before and after extraction. Deionized water was used for all experiments in this study.

Sample Digestion

A 100g xenotime sample was fused with 200g of NaOH pellets in a crucible at a temperature range of 300-400°C for 3 hours. The resulting sintered sample was then dissolved in 2000 mL of deionized water, stirred for 3 hours, and filtered using a vacuum filter. The precipitate was washed with deionized water until pH 7 was reached, and then dried in an oven at 70°C for 24 hours.

REE-Loaded Aqueous Solutions

A rare earth hydroxide (REOH) precipitate was obtained through drying. REE-loaded aqueous solution were prepared by leaching REOH into acetic acid with concentrations of 0.5, 1, 3, and 5 M. The solutions were stirred at a temperature range of 70-80°C for a specified period. The concentrations of Nd and Dy in the solutions before extraction were analyzed using EDXRF.

Solvent Extraction

A 30% extractant was prepared by dissolving a specific volume of D2EHPA in kerosene. The aqueous solutions were mixed with the extractant at ratios of 1:1 to 1:4 and stirred for 15 minutes at 30°C, 40°C, 50°C and 60°C. The mixture was then left to equilibrate for 20 minutes before separating into aqueous and organic phases. The composition of the organic phase was analyzed using EDXRF.

The extraction efficiency (%E) was calculated using Equation (1) to determine the percentage of solute that transfers from the aqueous to the organic phase. The equation defines extraction efficiency as the product of the distribution coefficient (D), and the volumes of the aqueous (V_A) and organic (V_O) phases.

$$\%E = \frac{D \text{ x } \frac{V_o}{V_A}}{1 + (D \text{ x } \frac{V_o}{V_A})} \text{ x } 100 \qquad (1)$$

The distribution coefficient (D) in Equation (2) is defined as the ratio of the element concentrations in the organic to the aqueous phases at the equilibrium state where Co is the concentration of an element in the organic phase and C_A is the concentration of an element in the aqueous phase.

$$D = \frac{C_O}{C_A} \qquad (2)$$

RESULTS AND DISCUSSION

Table 1 shows the concentration of REE before extraction in acid solution at the concentrations of 0.5, 1, 3 and 5M. The results showed that the concentrations of Dy and Nd in the xenotime samples were 5.19, 6.47, 6.57 and 6.89% and 0.59, 0.90, 1.19 and 1.06%, respectively. Notably, Dy concentrations were significantly higher than Nd concentrations due to xenotime's composition as a heavy rare earth element (HREE) phosphate. The solution also contained naturally occurring radioactive materials (NORM), with thorium (Th) and uranium (U) present at less than 1% composition each.

Table 1. REE concentration in acetic acid solution before extraction

REE	Atomic Number	REE Concentration (%)			
		0.5M	1M	3M	5M
HREE					
Y	39	69.55	71.46	66.86	68.26
Gd	64	2.30	2.73	2.35	2.32
Dy	66	5.19	6.47	6.57	6.89
Ho	67	1.18	1.78	1.48	1.65
Tm	69	1.21	1.32	1.38	1.03
Yb	70	4.60	4.77	7.33	7.00
LREE					
Nd	60	0.59	0.90	1.19	1.06
Sm	62	0.68	0.94	0.53	0.40
La	57	ND	0.44	0.63	0.66
NORM					
Th	90	ND	ND	0.15	0.14
U	92	0.55	0.99	0.29	0.22

Effect of CH_3COOH concentration

The effect of acid concentration on the extraction behavior of Dy and Nd was examined by varying the concentration of CH_3COOH from 0.5 M to 5 M at an O/A ratio of 1 and a temperature of 30°C. As shown in Fig. 1, the extraction efficiency increased when the acid concentration rose from 0.5 M to 1M, reaching 99.3% for Dy and 99.4% for Nd. According to Tang et al. (2019), the increase in extraction efficiency is attributed to the insufficient acid concentration, which fails to meet the process requirements. However, as the acid concentration continued to increase, the extraction efficiency of Dy and Nd decreased slightly to 95.1% and 92.9%. The results indicate that the extraction of Dy and Nd no longer increases when the concentration exceeds 1M, suggesting that the acid is sufficient to consume major elemental oxides and react with rare earth compounds at higher concentrations. Notably, partially encapsulated Nd and Dy have limited opportunities to interact with the acid, even when recovery is no longer limited by the lack of hydrogen ions (H+) (Cao et al. 2018).

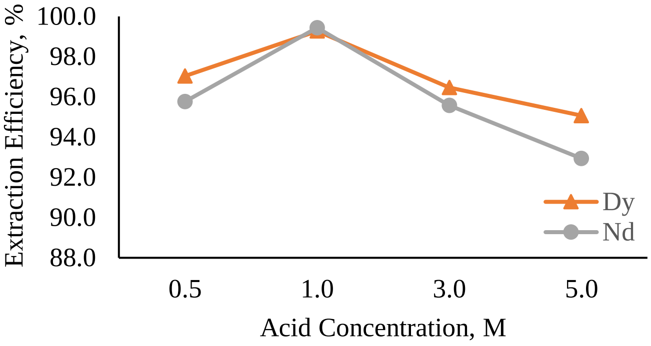

Figure 1. Effect of acid concentration on extraction efficiency

Effect of Aqueous-to-Organic Ratio

The aqueous-to-organic phase ratios (A/O) of 1:1, 1:2, 1:3, and 1:4 was examined to investigate their impact on the extraction of Dy and Nd under constant conditions. The results showed that the highest extraction efficiency was achieved at an A/O ratio of 1:1, with extraction yields of 99.3% for Dy and 99.4% for Nd. However, as the A/O ratio increased to 1:2, the extraction efficiency began to decline, as depicted in Figure 2. Specifically, at A/O ratios of 1:3 and 1:4, the extraction efficiencies for Dy and Nd were 95.5% and 95%, and 95% and 94%, respectively.

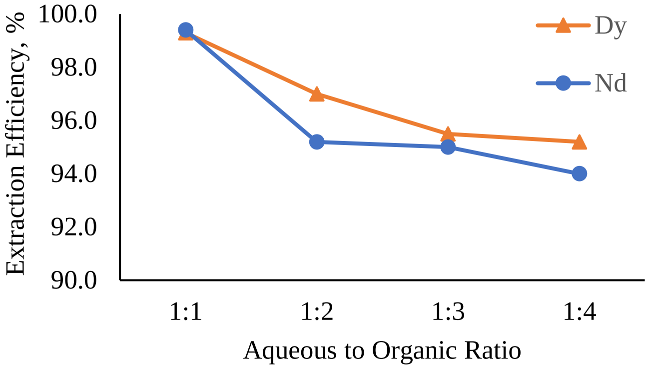

Figure 2. Effect of aqueous-to-organic ratio on extraction efficiency

The decrease in extraction efficiency is attributed to the solvent's saturation point being reached or exceeded, as suggested by Pusporini et al. (2021). Consequently, the declining trend in extraction efficiency observed in this study is due to the limitation of D2EHPA's ability to extract Dy and Nd at higher A/O ratios.

Effect of Temperature

The impact of temperature on extraction efficiency was examined at 30°C, 40°C, 50°C, and 60°C. The results showed that the extraction efficiency of Dy and Nd decreased from 99.3% and 99.4% to 90.2% and 90.1%, respectively, as the temperature increased from 30°C to 60°C as shown in Fig.3. This trend is consistent with findings from other studies (Arellano et al. 2020, Altansukh et al. 2021, Pan et al. 2022), which have reported that extraction activity using a temperature of 30°C is optimal for RE elements. Pan et al. (2022) also emphasized the importance of avoiding high temperatures above 35°C, as they can cause degradation of the extracted material, leading to decreased extraction efficiency and yield.

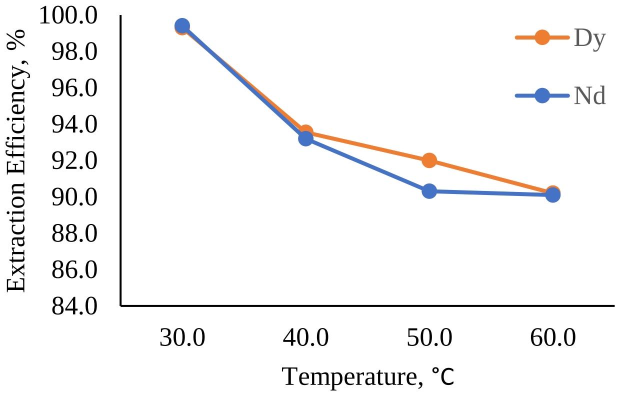

Figure 3. Effect of temperature on extraction efficiency

Therefore, selecting the suitable extraction temperature is crucial to maintain the stability of the extracted material, as excessive temperatures can destroy the structure and activity of the extraction process. As a result, increasing the extraction temperature does not significantly improve the extraction yield of Dy and Nd in this experiment.

CONCLUSION

This study demonstrates the successful extraction of Dy and Nd from an acetic acid leached solution of xenotime using 30% D2EHPA through solvent extraction. The results show that the leached solution concentration, aqueous-to-organic ratio, and temperature significantly impact the extraction efficiency of Dy and Nd. The optimal conditions for extraction were found to be a leached solution concentration of 1M, an extraction temperature of 30°C, and an aqueous-to-organic volume ratio of 1:1, resulting in extraction efficiencies of 99.3% for Dy and 99.4% for Nd. Overall, this study suggests that acetic acid has potential as a mineral leaching medium for the extraction of rare earth elements, providing a promising approach for the recovery of these valuable materials.

REFERENCES

Altansukh Batnasan, Ariunbolor Narankhuu, Ariuntuya Battsengel, Kazutoshi Haga and Atsushi Shibayama, (2021), Effect of Organic Extractants on the Extraction of Rare Earth Elements from Sulphuric Acid Leach Liquor, *Atlantis Highlights in Chemistry and Pharmaceutical Sciences*, 2:142-148.

Arellano Ruiz, V.C., Kuchi, R., Parhi, P.K. and Lee, J.Y., (2020), Environmentally friendly comprehensive hydrometallurgical method development for neodymium recovery from mixed rare earth aqueous solutions using organo-phosphorus derivatives, *Scientific Report*, 10: 16911.

Azhar, N., Takip, K., Hazan, R., W. and Sapiee N., (2020), Solvent extraction of thorium from Malaysian xenotime using tributyl phosphate (TBP), IOP Conference Series; *Materials Science and Engineering 785*.

Balaram, V., (2019), Rare earth elements: A review of applications, occurrence, exploration, analysis, recycling, and environmental impact, *Geoscience Frontier* 10: 1285–1303.

Cao, S., Zhou, C., Pan, J., Liu, C., Tang, M., Ji, W., Hu, T. and Zhang, N., (2018), Study on Influence Factors of Leaching of Rare Earth Elements from Coal Fly Ash, *Energy and Fuels*, 32(7): 8000–8005.

Dushyantha, N., Batapola, N., Ilankoon, I.M., Rohitha, S., Premasiri, R., Abeysinghe, B., Ratnayake, N. and Dissanayake, K., (2020). The Story of Rare Earth Elements (REEs): Occurrences, Global Distribution, Genesis, Geology, Mineralogy and Global Production, *Ore Geology Reviews* 122: 103521.

Farzaneh Sadri, Amir Mohammad Nazari, and Ahmad Ghahreman, (2017), A review on the cracking, baking and leaching processes of rare earth element concentrates, *Journal of Rare Earths* 35 (8): 739-752.

Gergoric, M., Barrier, A. and Retegan, T., (2019), Recovery of Rare-Earth Elements from Neodymium Magnet Waste Using Glycolic, Maleic, and Ascorbic Acids Followed by Solvent Extraction, *Journal of Sustainable Metallurgy* 5: 85–96.

Hazan, R., Kones, J., Takip, K., Sapiee, N., Azhar, N., and Paulus, W., (2019), Recovery of thorium and rare earth element (REE) from different particle size of xenotime mineral, *Journal Of Nuclear and Related Technologies* 16(02): 25-30.

Jacqueline, K., Norhazirah, A., Nur Aqilah, S., and Khaironie, M T., (2019). Alkaline Fusion of Malaysian Monazite and Xenotime for the Separation of Thorium and Uranium, *Jurnal Sains Nuklear Malaysia*, 31(1): 37 – 41.

Jowitt, S. M., Werner, T. T., Weng, Z. and Mudd, G. M., (2018), Recycling of the Rare Earth Elements, *Current Opinion in Green and Sustainable Chemistry* 13: 1−7.

Mancheri, N.A., Sprecher, B., Bailey, G., Jianping Ge, J. and Tukker, A., (2019), Effect of Chinese policies on rare earth supply chain resilience, *Resources, Conservation and Recycling* 142: 101-112.

Mnculwane, H.T., (2022), Rare Earth Elements Determination by Inductively Coupled Plasma Mass Spectrometry after Alkaline Fusion Preparation, *Analytica*, 3(1):135-143.

Pan-Pan Sun, Do-Hyeon Kim, and Sung-Yong Cho, (2018), Separation of neodymium and dysprosium from nitrate solutions by solvent extraction with Cyanex272, *Minerals Engineering* 118: 9-15.

Pusporini, N.D., Sediawan, W.B., Wahyu Rachmi Pusparini, W.R., Ariyanto, T. and Sulistyo, H., (2021), Equilibrium analysis of neodymium - yttrium extraction in nitric acid media with D2EHPA as solvent, *Chemical Thermodynamics and Thermal Analysis*, 1–2:100006.

Sanjith Udayakumar, Norlia Baharun, Sheikh Abdul Rezan, Aznan Fazli Ismail, Khaironie Mohamed Takip, (2021), Economic evaluation of thorium oxide production from monazite using alkaline fusion method, *Nuclear Engineering and Technology* 53(7): 2418-2425.

Stein, R.T., Kasper, A.C.and Veit, H.M., (2022), Recovery of Rare Earth Elements Present in Mobile Phone Magnets with the Use of Organic Acids, *Minerals*,12: 668.

Tang, X., Zhang, Y., Liu, J., Zhang, S., and Wang, F., (2019), Enhanced bioactive compound extraction from spent coffee grounds using ultrasound-assisted extraction and response surface methodology, *Food Chemistry*, 295, 124-132.